Technical report; TR-251

KNMI

Analysis of global irradiance measurements from pyranometer and AVHRR

G.J. van Geel, R. Roebeling and A.J. Feijt

De Bilt, 2003

Technical Report = Technisch Rapport; TR-251

De Bilt, 2003

PO Box 201, 3730 AE De Bilt
The Netherlands
Wilhelminalaan 10
http://www.knmi.nl
Telephone +31 30 22 06 911
Telefax +31 30 22 10 407

Authors: G.J. van Geel
R. Roebeling
A.J. Feijt

UDC: 551.501.721
551.507.321.1
551.521.1

ISSN: 0169-1708

ISBN: 90-369-2231-3

● ● ● ●

Analysis of Global Irradiance Measurements from Pyranometer and AVHRR

G.J. van Geel
R. Roebeling
A.J. Feijt

April, 2003

This study is based on work done at the Royal Netherlands Meteorological Institute (KNMI) on behalf of the author's Master of Science degree in Meteorology and Air Quality at Wageningen University.

"I've looked at clouds from both sides now,
from up and down and still somehow
It's clouds' illusions I recall.
I really don't know clouds at all..."

From Joni Mitchell's classic song,
"Both Sides Now,"

Contents

Summary

This thesis is about analysis of the accuracy of downwelling solar surface irradiance (DSSI) retrieval schemes for satellites with ground-based measurements for different atmospheric conditions. A two-step retrieval scheme is used to obtain DSSI values from satellite measurements. The first step of the retrieval scheme uses bi-directional reflectivities as input to obtain narrowband cloud optical depths. The second step uses these cloud optical depths to obtain broadband atmospheric transmissivities (BAT). However, a conversion from narrowband to broadband cloud optical depths has to be made first. At the end of this two-step approach, the BAT is used to calculate DSSI. Inversely, the second step is used in order to obtain broadband cloud optical depths from derived BAT values measured by the pyranometer.

For the interpretation of the AVHRR channel 1 reflectivity and the pyranometer BAT, calculations are performed on mean atmospheric state. Look up tables (LUTs) store values of both the 0.63 μm bi-directional reflectance and the BAT as calculated for a wide range of satellite viewing geometries and solar zenith angles for 14 values of cloud optical depths. For a single satellite pixel, multilinear interpolation in the geometrical parameters and the vertically integrated water vapour is used to extract the corresponding pairs of reflectance/ transmissivity for a given measurement at all values of cloud optical depth included in the LUTs. Then, the relation of reflectance and transmissivity is established by bicubic spline interpolation and the transmissivity corresponding to the AVHRR channel 1 measurement is determined.

Three cases representing three different atmospheric conditions are analysed. These cases, which are referred to as 'clear sky', 'overcast', and 'broken clouds' are selected on their cloud cover faction. The clear sky case acts as a reference case, since it is not complicated by the variability of clouds and their optical properties introduces large uncertainties in the modelling of cloudy atmosphere. As a consequence, clear sky observations provide the most reliable reference case for evaluating the representation of the interaction of radiation with atmospheric aerosols and gases in a radiative transfer model (RTM) (Deneke, 2002).

The clear sky case shows that the satellite retrieval yields results that agree with independent pyranometer measurements. The bias is 17.1 W m^{-2}. This is 2.5% of the mean. A significant part of the bias could be attributed to an offset in calculating the solar zenith angle. After correcting for this offset, the bias is reduced to 2.9 W m^{-2}, which is 0.4% of the mean. Atmospheric constituents, e.g. aerosol concentration and water vapour that dominates the solar flux during clear skies, are highly variable in time and space. This results in a RMSE of 0.017 that is 2.3% of the mean BAT. This variability is not accounted for in the retrieval scheme in its current form. This is a limitation, but also marks the boundaries of the satellite retrieval.

The most important parameter determining the atmospheric transmissivity in cloudy atmosphere is the cloud optical depth. The variability in water vapour and aerosol concentration is less important in a cloudy atmosphere. The results of the overcast case show that discrimination between precipitation and non-precipitation cases is desirable. Comparison of measured and retrieved quantities show no correlation if precipitation was recorded. For the non-precipitation case, retrieval results are in agreement with the ground-based measurements. A correlation of 0.89 between retrieved and measured DSSI is found.

Comparing satellite measurements with ground-based observations is difficult in case of broken clouds. In all comparisons of this broken cloud case the problem of collocation occurs. *In situ* pyranometers measure continuously in time, while the AVHRR instrument measures instantaneously a spatial distribution. When comparing ground and satellite quantities, measured or retrieved, it is always questionable which part of the time series corresponds to which part of the spatial distribution.

The observed deviations between pyranometer measured and satellite retrieved DSSI are of fundamental nature, as the static view of a cloud field assumed in the retrievals does not reflect all aspects of real clouds. Broken clouds show significant variability in time and space (4D). Therefore, results of this case study are difficult to interpret within the boundaries of a 1D radiative transfer model, used in this thesis.

1. Introduction

1.1 Motivation

Satellites play a crucial role for collecting data and conducting research, which will help improve both the knowledge of the current state of the Earth's atmosphere as well as our understanding of human-induced and naturally occurring changes of the atmosphere.

Shortwave (SW) radiative fluxes at the Earth's surface are of primary interest in climate research, because they control the total energy exchange between the atmosphere and the surface. Monitoring surface SW irradiance is also useful in other research areas, such as primary productivity and global carbon cycling (Bréon *et al.*, 1994). The latter is an important factor on research in global warming. Instruments carried on satellites obtain information on these SW fluxes.

Current models for deriving downward solar surface irradiance (DSSI) from satellite observations are implemented on local or, at most, regional scales (Pinker & Laszlo, 1992). As these radiative transfer models (RTMs) become more sophisticated; the demand for improved representation of their input parameters increases too.

Recent investigations have found large deviations in measurements for the incident solar radiation at the surface, which has lead to an ongoing debate about the accuracy of current measurements and RTMs. Comparison of the retrieved and measured quantities has to been done to validate such models. An important part of satellite remote sensing research is the task of validation of the derived products, to make sure that they provide a consistent picture together with traditional surface measurements (Deneke, 2002).

1.2 Objective of this study

This research aims to analyse the accuracy of a satellite retrieval scheme setup by Deneke (2002) that retrieve cloud optical depths from pyranometer and satellite measurements to calculate downwelling solar surface irradiances. Analysis is performed for different atmospheric conditions.

1.3 Structure

A theoretical framework of the relevant parts of radiative transfer theory is presented in Chapter 2. Ch. 3 gives a description of the instruments used for analysis, together with an introduction of the retrieval method used for deriving downwelling solar surface irradiance from satellite measurements. Results of several case studies are given in Ch. 4. The principle conclusions of this thesis are summarized and an outlook to possible extension of the work is given in Ch. 5.

2. Background

Life is not possible without energy! Energy exists in many forms and it is the basis of all there is. This chapter discusses some of the characteristics of electromagnetic energy which are relevant to satellite remote sensing. This chapter is divided into seven sections. The first six sections introduce basic radiation theory, e.g. black body radiation, radiation laws and definitions. It is based on standard literature, i.e. Goody & Yung (1989), Peixoto & Oort (1972), Lenoble (1973), and Liou (1980). Other literature will be mentioned explicitly.

The last section introduces a theoretical radiative framework. This framework describes the most important atmospheric radiative processes occurring in clear sky and in cloudy atmosphere. This framework will be the basis of the retrieval method outlined in the following chapter. First, the basic principles of energy are introduced.

2.1 Energy

Electromagnetic (EM) radiation is one of the most important processes responsible for transporting energy in the atmosphere. This form of radiation travels in waves at the speed of light c (2.9973 x 10^{-8} m s^{-1} in a vacuum). It can be characterized by the wavelength of propagation λ or by the frequency ν (cycles s^{-1}), which are related by the expression $\lambda\nu = c$. The EM spectrum, as seen in Fig. 2.1, covers a wide range of wavelengths and can be divided into a number of spectral regions.

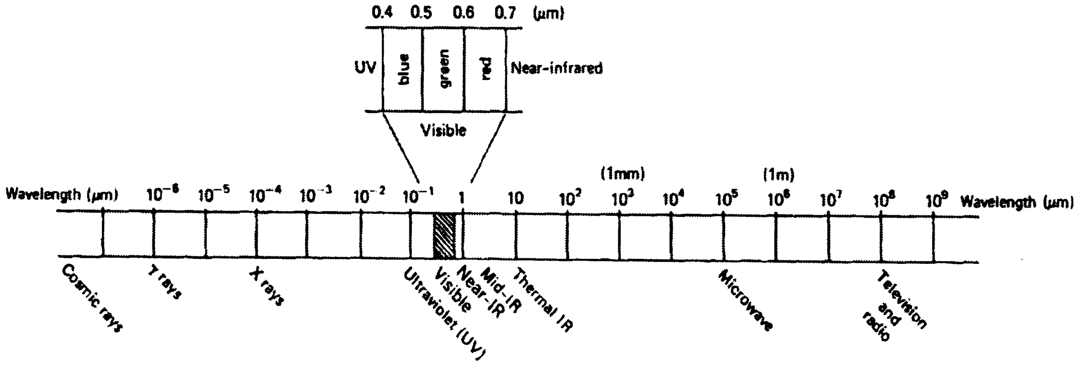

Figure 2.1: The electromagnetic spectrum, classified by wavelength.

The spectrum exists of γ, x-rays, visible, infrared, and radar waves. Most of the energy of the Sun is contained between wavelengths of 0.1-4 µm and consists of ultraviolet (0.001-0.4 µm), visible (0.4-0.75 µm) and near infrared radiation (0.75-5 µm). Further, it is useful to split up radiation into shortwave (solar) and longwave (terrestrial) radiation. The reason for this separation will be described in Section 2.4. The two forms of radiation will be introduced first.

2.2 Radiation

The solar radiation covers the entire EM spectrum. However, the most significant portion of the spectrum associated with radiative energy transfer in the climate system ranges from the ultraviolet to the near infrared, as mentioned in Section 2.1.

Essentially all energy that enters the Earth's atmosphere comes from the Sun since the upward conduction of heat from the Earth's interior (due to radioactive decay) is negligible (Peixoto & Oort, 1992). The incoming solar radiation is partly absorbed, partly scattered, and partly reflected by the various gases of the atmosphere, aerosols, and clouds. The remainder that reaches the Earth's surface is largely absorbed by the oceans, lithosphere, cryosphere, and biosphere.

In order to maintain the Earth in its long-term observed state of quasi-equilibrium, the amount of absorbed energy must be balanced by an equal amount of energy moving into outer space. The outgoing energy is also in the form of radiant energy emitted by the Earth's surface and atmosphere. In fact, we know that all bodies having a temperature above absolute zero K emit radiant energy over a large range of wavelengths. As we will see in Section 2.4, the higher the temperature of the emitting body, the larger the amount of emitted energy.

Since the solar radiation comes from a very distant point-like source, the Sun, it can be treated as parallel unidirectional radiation. On the other hand, the terrestrial radiation comes from all directions since each molecule acts as an individual "minuscule Sun" for thermal diffuse radiation. Furthermore, the terrestrial emission is negligible at the wavelengths of solar emission so that only absorption has to be considered. However, emission and absorption are equally important at the frequencies of terrestrial radiation and need to be considered simultaneously.

2.3 Definition of Solar constant, Radiance, and Irradiance

Solar constant

The solar constant S is defined as the amount of solar radiation incident per unit area and per unit time on a surface normal to the direction of propagation and situated at the Earth's mean distance from the Sun. As this distance is large compared to the radius of the Sun, the incident radiation can be considered as a parallel beam. At the mean distance, the solar constant S is approximately 1367 ± 5 W m^{-2}. This is calculated for the spectral range of the Sun.

However, the solar constant S is not really a constant, since the distance between the Earth and the Sun differs periodically. This is due to the shape of the Earth's orbit around the Sun, which is not perfectly circular. That means that the radius of the Earth's orbit reaches a minimum and maximum value. The variation in solar radiation reaching the top of atmosphere (TOA) is described by Eq. 2.1 through the inverse square law

$$f(d) = (d_m / d)^2, \tag{2.1}$$

where d is the actual distance and d_m the mean distance between the Sun and the Earth. The ratio $(d_m/d)^2$ varies from 1.0344 on 3rd of January to 0.9674 on 5th of July.

Radiance

The number of photons carrying an energy dE that reach a surface out of a solid angle element $d\Omega$ is proportional to the time of exposure dt, the surface area ds and the width $d\lambda$ of the spectral range considered. The spectral radiance I_λ is therefore defined as

$$I_\lambda \equiv \frac{dE}{ds\,dt\,d\lambda\,d\Omega}. \tag{2.2}$$

The surface area ds either has to be oriented perpendicular to the propagation direction of the photons, or both the area ds and the solid angle $d\Omega$ have to be treated as vector quantities with lengths equal to their sizes and directions normal to their orientation. A tilt of angle θ_0 between ds and $d\Omega$ is then accounted for by the scalar product of both vectors, resulting in

$$I_\lambda(\theta) = \cos(\theta_0) I_\lambda = \mu I_\lambda, \tag{2.3}$$

where μ denotes the cosine of the angle θ_0.

Irradiance

The spectral irradiance, also referred to as net flux, is a measure for the net energy transported through a given unit surface per unit time and wavelength interval, and can be derived by integrating the contribution of radiance from a particular direction over the full hemisphere according to

$$F_\lambda \equiv \int_\Omega I_\lambda \cos(\theta_0) d\Omega = \int_{-\pi/2}^{\pi/2} \int_0^{2\pi} I_\lambda \sin(\theta)\cos(\theta) d\phi d\theta = \int_{-1}^{1} \int_0^{2\pi} I_\lambda \mu d\phi d\mu. \tag{2.4}$$

Here, the integration over the total hemisphere has been split into integrations over the cosine of the zenith angle μ and the azimuth angle ϕ. The value of $\cos\theta_0$ for any location and time may be computed as

$$\cos\theta_0 = \sin\varphi\sin\delta + \cos\varphi\cos\delta\cos h, \qquad (2.5)$$

where φ is the latitude, δ is the solar declination, and h is the hour angle (in radians) from the local meridian. The irradiance F at the TOA depends on the Earth-Sun distance but also on the Sun's zenith angle θ_0

$$F_{TOA} = Sf(d)\cos\theta_0, \qquad (2.6)$$

where F_{TOA} is the flux at TOA and S is the solar constant. Together with Eq. 2.1 and the atmospheric transmissivity parameter t_λ, we can now express the equation for calculating downwelling solar irradiance at the surface

$$F_{sfc} = Sf(d)\cos\theta_0 t_\lambda, \qquad (2.7)$$

where F_{sfc} and S are given in units W m^{-2}. Eq. 2.7 highly depends on the transmittance of the Earth's atmosphere and on the angle of shortwave radiation penetrating the atmosphere.

2.4 Thermal emission and Radiation Laws

Thermal emission is the inverse of absorption and is the dominant source of radiation originating from both the Sun and the Earth (Thomas & Stamnes, 1999). Every particle of matter at a temperature greater than absolute zero contains excited quantum states. The spontaneous decay of these states is accompanied by the creation of radiative energy. The temperature of the source, as well as the source's efficiency for emitting radiation determines the intensity and spectral distribution of this radiative energy. The latter is described by Planck in 1901.

Planck's Law

Planck's Law implies that if temperature increases, the radiance also increases; the percentage increase varies as a function of wavelength λ, and temperature T. By definition, a black body is a perfect absorber. It also emits with the maximum possible efficiency. For such a black body, the emitted radiance is only a function of temperature and wavelength, and is given by Planck's Law

$$I(T,\lambda) = \frac{2\pi hc^2}{\lambda^5}\cdot\frac{1}{e^{hc/\lambda kT} - 1}, \qquad (2.8)$$

in W m^{-2} Å^{-1}, where

h = Planck's constant (6.266 x 10^{-34} J s)
k = Boltzmann's constant (1.38 x 10^{-23} J K^{-1})
c = velocity of light (3 x 10^8 m s^{-1})
λ = wavelength of energy (1 Å = 10^{-10} m)
T = absolute temperature of the black body (deg K)

Stefan-Boltzmann Law

Eq. 2.1 is written for one wavelength λ. It can be rewritten for all wavelengths to give the total power radiated per unit area of a black body

$$F = \int_0^\infty F(T)d\lambda = \frac{2\pi^5 k^4}{15c^2h^3}T^4, \tag{2.9}$$

in W m^{-2}. The first component of the right hand side of Eq. 2.9 consists entirely of constants (π, k, c, h), so the equation can be simplified to

$$F = \sigma T^4, \tag{2.10}$$

which is the Stefan-Boltzmann law and σ (= 5.67 x 10^{-8} W m^{-2} K^{-4}) is the Stefan-Boltzmann constant.

Wien's Displacement Law

The temperature of an object determines the wavelength of maximum EM energy emission. Wien's Displacement law describes this theory as

$$\lambda_{\max} = \frac{a}{T}, \tag{2.11}$$

where λ_{max} is the wavelength of maximum energy emission in μm, T is the temperature of the object in deg K, and a is a constant (2898 μm K). By using Wien's law the temperature of a remote object can be measured by observing its spectrum and identifying the wavelength of maximum energy emission (λ_{max}). The hotter the body then the shorter the wavelength of maximum energy emission.

The solar radiation closely follows the spectrum of a black body having temperatures between 6000 and 5700 K, which peaks in intensity at a wavelength of 0.470 μm but which spans the range from less than 0.2 μm to greater than 1.8 μm. The radiation energy emitted by the Earth corresponds approximately to black body radiation. Its effective radiative temperature is found to be about 255 K, which peaks in intensity at a wavelength of around 11 μm. This is well within the range of temperatures observed at the surface and within the Earth's atmosphere.

The large difference in temperature of the Sun and the Earth allows a separate treatment of radiation originating from the Sun, and radiation emitted by the Earth's atmosphere and the surface. This is illustrated in Fig. 2.2.

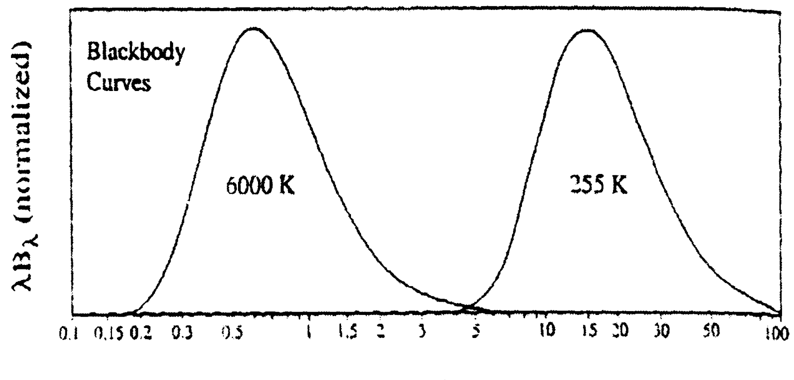

Figure 2.2: Peak-normalized radiation spectrum from bodies with a temperature of 6000 K and 255 K. (From: Thomas & Stamnes, 1999)

As seen in Fig. 2.2, a combination of radiation emitted by the Sun and the Earth spans a range from less than 0.2 μm to greater than 50 μm. However, the two radiative spectral curves exhibits very little overlap. For this reason we refer to radiation emitted by the Sun as *shortwave radiation* and radiation emitted by the Earth and its atmosphere as *longwave radiation*. The two spectral curves are separated arbitrarily at 4 μm.

Kirchhoff's Law

The previous laws deal essentially with the intensity emitted by a black body. However, in general, a medium will not only absorb but also reflect part of the incident radiation and transmit the remainder. Thus, in terms of the ratios of the absorbed, reflected, and transmitted radiation with respect to the monochromatic intensity of the radiation I_λ incident upon a layer, we may write

$$a_\lambda + r_\lambda + t_\lambda = 1, \tag{2.12}$$

where $a_\lambda = I_{\lambda a} / I_\lambda$ is the absorptivity, $r_\lambda = I_{\lambda r} / I_\lambda$ the reflectivity (or albedo at wavelength), and $t_\lambda = I_{\lambda t} / I_\lambda$ the transmissivity of the layer.

Kirchhoff's law states that in thermodynamic equilibrium and at a given wavelength the ratio of the intensity of emission I_λ to the absorptivity a_λ of any substance does not depend on the nature of the substance. It depends only on the temperature and the wavelength:

$$I_\lambda / a_\lambda = f(\lambda, T). \tag{2.13a}$$

In case of a black body $a_\lambda = 1$ for all values of λ. Therefore, the ratio $f(\lambda,T)$ is equal to $F(T)$, the black body intensity for a given temperature and wavelength. For any real body a_λ is less than 1, so that $I_\lambda < F(T)$. When a_λ is the same at all wavelengths we define what is known as a grey body.

In order for I_λ to be different from zero it is necessary that both $F(T)$ and a_λ be different from zero. Thus, for a body to be able to emit energy at a given wavelength and at a given temperature it is necessary that a black body also emit energy at that temperature and that the body be able to absorb it. Since the emissivity ε_λ is defined as the ratio of the emitted intensity to the Planck function, Kirchhoff's law can also be expressed by

$$\varepsilon_\lambda = a_\lambda, \tag{2.13b}$$

so that any selective absorber of radiation at wavelength λ is also a selective emitter of radiation at the same wavelength.

Beer-Bouger-Lambert Law

This law expresses the change in radiation intensity I_λ due to the absorption of the radiation. Let us consider a parallel beam of radiation with intensity I_λ passing through an absorbing medium, such as shown in Fig. 2.3.

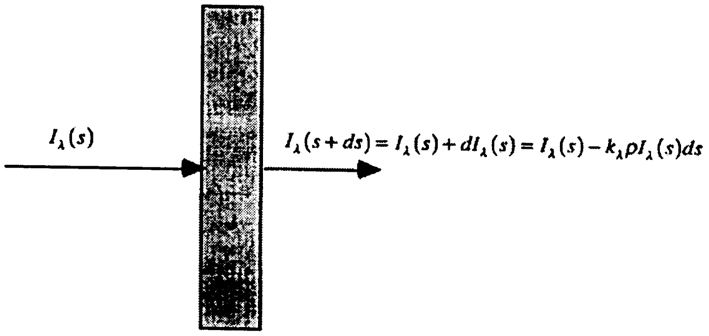

Figure 2.3: Beer-Bouger-Lambert Law

The intensity of radiation after traversing a layer of thickness ds in the direction of propagation is $I_\lambda + dI_\lambda$, and

$$dI_\lambda = -k_{\lambda a} I_\lambda \rho ds, \tag{2.14}$$

where ρ is the density of the medium and $k_{\lambda a}$ is the absorption coefficient (absorption cross section in units of area per unit mass) for radiation of wavelength λ. Integration of this equation between $s = 0$ and $s = s_1$ yields the emergent intensity $I_\lambda(s_1)$ so that

$$I_\lambda(s_1) = I_\lambda(0)\exp\left(-\int_0^{s_1} k_{\lambda a}\rho ds\right), \tag{2.15}$$

where $I_\lambda(0)$ is the intensity at $s = 0$. When the medium is homogenous, $k_{\lambda a}$ is independent of s, and Eq. 2.15 then expresses the Beer-Bouger-Lambert absorption law.

2.5 Geometrical Setup

Fig. 2.4 is showing the necessary angles of viewing to describe radiative transfer in the atmosphere.

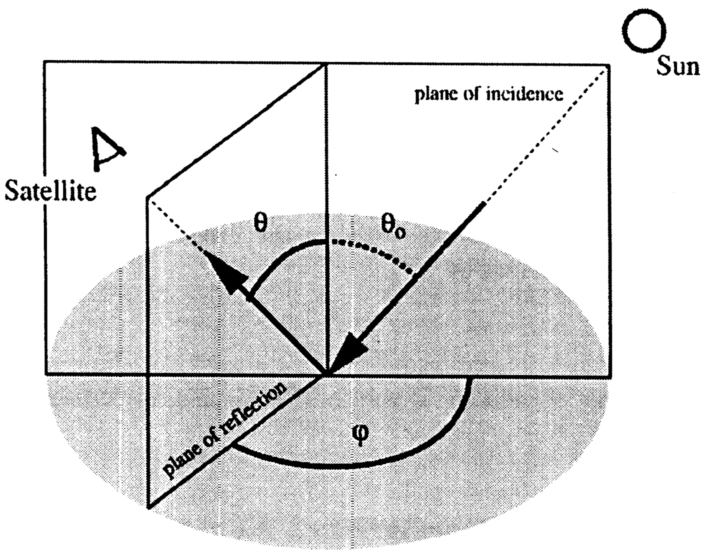

Figure 2.4: Schematic description of the Sun-satellite scattering geometry (From: Feijt, 2000).

The Sun's position in the sky can be specified by two angles, which are chosen as the solar zenith angle θ_0 and the azimuth angle ϕ here. The solar zenith angle represents the angle between the plane of solar incidence and the normal to the Earth's surface. The parameter μ denotes the cosine of the solar zenith angle. In degrees, 0 means straight up and 180 is straight down, which gives μ values of 1 and −1, respectively. The azimuth angle, ϕ, is defined as the angle between geographic north and the projection of the Sun on the Earth's surface in clockwise direction. The position of a satellite can be described likewise by its zenith and azimuth angles θ_s and ϕ_s.

2.6 Phase Function

The phase function, $P(\theta)$, is the amount of energy at an angle θ relative to the direction of propagation of the incident light. For spherical particles, as well as an average of randomly orientated particles, it is independent of the direction of incidence, and only a function of scattering angle θ. The latter is illustrated in Fig. 2.5.

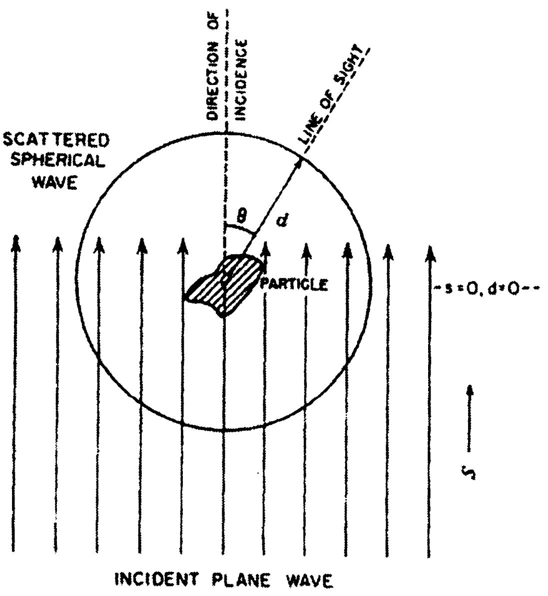

Figure 2.5: Definition of scattering angle θ (From: Goody & Yung, 1989).

As a probability, the phase function P is normalized to unity according to

$$\frac{1}{4\pi}\int_{\Omega} P_{\Omega}(\theta)d\Omega = 1. \tag{2.16}$$

An angle θ close to 0° means scattered light propagated in nearly the same direction as the non-scattered light; this is referred to as "forward scattering". The angle $\theta = 180°$ describes light being scattered back into the direction of the primary source; this is called "backward scattering". This scattering principle is described by the asymmetry parameter, g. If $g = 1$ all light is scattered forwards, if $g = -1$ all light is scattered backwards. For isotropic (i.e. light is scattered symmetrically between the forward and backward directions) and Rayleigh scattering: $g = 0$. For example, the asymmetry parameter for aerosol have values mostly around 0.6 – 0.7. The larger the aerosol particle, the larger g becomes.

So far, individual parameters are described, which outline radiative processes in the Earth's atmosphere. The following section uses this theory to explain important radiative processes in the Earth's atmosphere for different atmospheric conditions.

2.7 Shortwave Atmospheric Radiative Transfer

2.7.1 Radiative Transfer Equation

The interaction of radiation with a medium such as the atmosphere is formally described by the radiative transfer equation (RTE), given by

$$\mu \frac{dI_\lambda(\tau,\mu,\phi)}{d\tau} = -I_\lambda(\tau,\mu,\phi) + J_\lambda(\tau,\mu,\phi), \tag{2.17}$$

where I_λ is the spectral radiance, J_λ the source function, and μ and ϕ are the cosine of the zenith angle, and the azimuth angle, respectively. This form of RTE uses the optical depth τ as the vertical coordinate, and is limited in applicability to plane-parallel atmospheres.

Generally, the components contributing to the source function are emission as well as scattering of both direct and diffuse radiation. For the shortwave region, emission within the atmosphere can be neglected as mentioned earlier.

The source function is given by

$$J_\lambda(\tau,\mu,\phi) = \frac{\omega}{4\pi} \int_0^{2\pi} \int_{-1}^{1} I_\lambda(\tau,\mu',\phi') P_\lambda(\mu,\phi;\mu',\phi') d\mu' d\phi', \tag{2.18}$$

where ω is the single-scattering albedo, which specifies the probability of a photon to be scattered in case of an interaction with the atmosphere. These two equations specify the physical constraints imposed on a radiance field by Maxwell's equations for plane-parallel media without internal sources of radiation.

Numerical solutions of the RTE

For an atmosphere with known optical properties and given boundary conditions, the desired radiative quantities can be calculated from the corresponding solution of Eq. 2.17. Hence, a way of solving this equation is required for given optical properties and boundary conditions. Unfortunately, there exists no general analytical solution to the RTE. Several techniques have been developed to find numerical approximations. A short summary of the Discrete-Ordinates method used for the calculations presented within this thesis is given here.

General Simplification
First, the direct beam irradiance F_{DIR} is calculated for the complete atmosphere. The irradiance of the direct beam is reduced according to the absorption Law of Lambert-Beer (see Eq. 2.15). This equation is a solution of the RTE in the absence of scattering and internal radiation sources. A pseudo source term is then added to the RTE, which accounts for the scattering of the direct beam irradiance at a given height. This allows the separate solution of the RTE for the direct and the diffuse radiance fields.

Discrete Ordinates Method
The Discrete Ordinates method for solving the RTE has been proposed by Chandrasakher (1960). The model atmosphere is subdivided into layers having homogenous optical properties.

A Fourier expansion of the azimuthal dependence of the diffuse radiance field and an expansion of the phase function in Legendre polynomials results in an infinite series of equations that are independent of the azimuth angle. The series is truncated considering enough equations to achieve the desired accuracy (Deneke, 2002).

Choosing a number of representative zenith angles according to a Gaussian quadrature with corresponding weights, the zenith angles dependence of each equation can be separated into a set of non-homogeneous differential equations. The number of zenith angles is called the number of streams, and is often chosen equal to the number of equations used for describing the azimuthal dependence. The solution for each atmospheric layer is a linear combination of the homogeneous solutions of these equations, plus a particular solution for the source term. The linear coefficients for a specific problem are fixed by the boundary conditions at the TOA and the surface, as well as the requirement of continuity of the radiance field at the layer boundaries.

While discussing the solution of the RTE, the knowledge of the optical properties of the Earth's atmosphere has been assumed. The following two paragraphs present how these properties interact with shortwave solar radiation. Based on the case studies presented in chapter 4, a clear-sky and a cloudy atmosphere are chosen to outline radiative transfer theory.

2.7.2 SW Radiation behaviour in a clear-sky atmosphere

Fig. 2.6 gives a schematic view of the radiative processes in the Earth's atmosphere for both shortwave and longwave radiation. As the solar radiation enters the atmosphere it is depleted by absorption and scattering. The absorbed radiation is directly added to the heat budget, whereas the scattered radiation is partly returned to space and partly continues its path through the atmosphere where it is subject to further scattering and absorption before it reaches the Earth's surface.

The combination of scattering and absorption is called extinction. Within the clear-sky atmosphere (i.e. zero clouds), extinction is mainly due to molecules and aerosol particles.

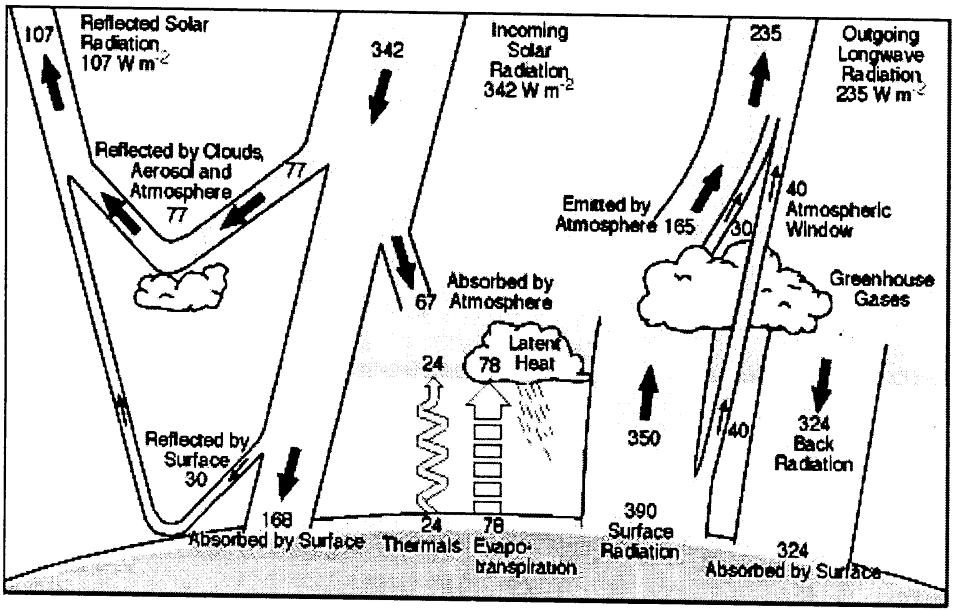

Figure 2.6: Schematic view of the Earth's radiation budget. Source: Kiehl and Trenberth (1997).

Concerning these interactions, the following parameters are important for radiative transfer in a clear sky atmosphere:

- Scattering
- Absorption
- Aerosols
- Surface albedo

Scattering

Scattering is a physical process by which a particle in the path of an EM wave continuously abstracts energy from the incident wave and reradiates that energy in all directions. It occurs at all wavelengths covering the entire EM spectrum. Although the frequency of the scattered radiation does not change, its phase and polarization may change substantially from those of the incident radiation.

Scattering occurs for particles of all sizes, including air molecules. Raleigh developed the scattering theory for particles with diameter that are small compared with the wavelength of the incident radiation. However, for particles whose sizes are comparable to or larger than the wavelength, the scattering is customarily referred to as Mie scattering. This form of scattering will be introduced in paragraph 2.7.3.

Rayleigh showed that the amount of scattering is inversely proportional to the fourth power of the wavelength ($\sim\lambda^{-4}$), so that the shorter the wavelength the more radiation will be scattered. Thus we may explain that the blue colour of the sky is due to the more intense scattering by the atmospheric molecules in the blue than in the red part of the spectrum. In fact, the sky is made visible through the scattering process. On the other hand, sunsets and sunrises appear reddish because the shorter (blue) wavelengths in the direct light are removed by scattering during the long path through the atmosphere, leaving the remaining reddish colour of the spectrum. Rayleigh's functional form is given by

$$I_\lambda(\theta) = I_{0,\lambda}\frac{8\pi^4 n\alpha}{\lambda^4 r^2}\left(1+\cos^2\theta\right), \qquad (2.19)$$

where $I_{0,\lambda}$ is the incident intensity, $I_\lambda(\theta)$ the scattered intensity, n and r the number density and radius of the scatterer and α the polarizability of the molecule. The scattered intensity, $I_\lambda(\theta)$, is a function of the scattering angle θ (see Section 2.6).

Absorption

Fig. 2.7 is showing the solar spectrum together with a number of absorption lines and bands (indicated in black), some resulting from absorption in the Sun's atmosphere and others from absorption by the gases of the Earth's atmosphere.

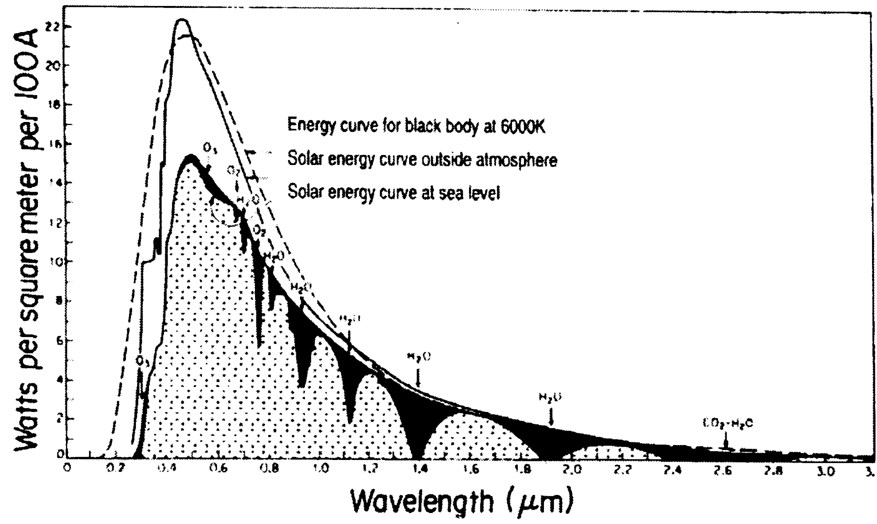

Figure 2.7: Spectral energy curves of solar radiation at sea level and extrapolated outside the atmosphere. The darkened areas illustrate gaseous absorption bands while the unshaded area represents Rayleigh scatter effects. Modified from Lacis and Hansen (1974) by Stephens (1984).

The solar irradiance is attenuated on its path through the atmosphere due to scattering and absorption. Therefore, the irradiance spectrum as measured at sea level for cloud free conditions (the lower curve in Fig. 2.7) deviates considerably from the TOA.

The absorption of radiation in gases occurs at specific wavelengths according to their atomic and molecular structure. At wavelengths shorter than 0.3 μm, oxygen and nitrogen absorb nearly all-incoming solar radiation in the upper atmosphere. However, between 0.3 and 0.8 μm, little gaseous absorption occurs. Only weak absorption by ozone takes place in this spectral range. This is obvious, because these are the wavelengths in which the solar radiation peaks. Aerosols also contribute to a lesser extent to absorption. At wavelengths of less than 0.8 μm, Rayleigh scattering of shortwave radiation back to space depletes the available flux.

Aerosols

When solar radiation penetrates into the Earth's atmosphere, it is absorbed and scattered not only by atmospheric gases (as stated above), but also by aerosols. Aerosols are defined as suspensions of liquid or solid particles in the air, excluding cloud particles and precipitation. The aerosols can be classified according to their origin, size, and atmospheric distribution. The very small particles with mean radius (000.1 to 0.1 μm) are called Aitken particles, the particles between 0.1 and 1 μm large particles, and those between 1 and 10 μm giant particles.

The aerosol particles in the air are due to two processes: (1) direct injection of dust, soot, sea salt particles, etc., from volcanoes, forest fires, human activities, and other natural processes, and (2) chemical reactions of gaseous materials within the atmosphere, such as the transformation of SO_2 into HSO_4 or sulphates, NO_x into nitric acids, and so on. These processes influence climate in two ways: (1) aerosol particles can alter the solar energy by absorbing or scattering the radiation both in cloud-free and cloudy conditions, thereby affecting the energy balance of the Earth and (2) the particles can serve as condensation and freezing nuclei playing an important role in the process of cloud formation and precipitation.

The representation of aerosols in radiative transfer models requires the extinction, single scattering albedo and phase function to be specified as a function of height and wavelength. In principle, they can be determined from the size distribution and aerosol composition by Mie calculations. In reality, both microphysical and optical properties of aerosols are difficult to measure and exhibit a strong spatial and temporal variability.

Surface Albedo

The basic definition of albedo is: albedo = outgoing irradiance / incoming irradiance. The surface albedo, the amount of radiation reflected at the surface, is an important quantity for radiative transfer as it specifies the boundary conditions at the surface. Surfaces that are independent of the direction of incidence and reflection are called Lambertian or isotropic.

The surface albedo is also important for modelling clouds, as radiation can be reflected multiple times between the surface and cloud layers. Its magnitude can vary significantly with wavelength and direction of incidence, depending on the type of surface. This is illustrated in Fig. 2.8. Further details on surface albedo for different surfaces are given in Appendix B.

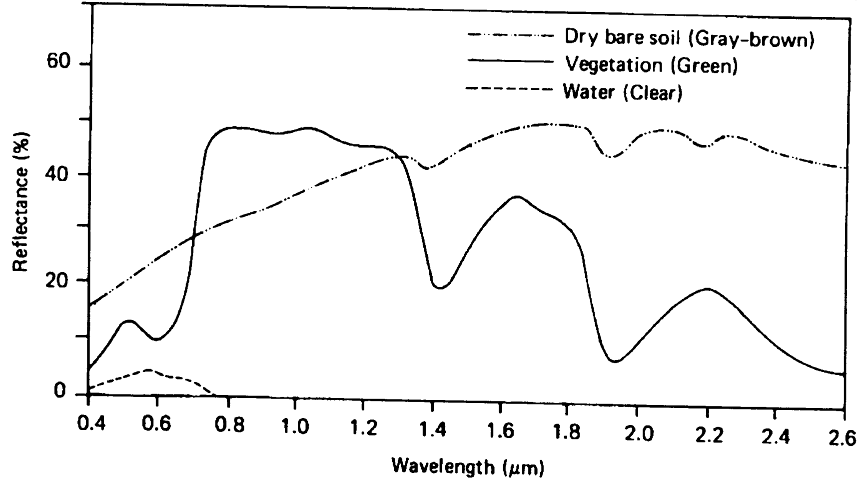

Figure 2.8: Typical reflectance curve for vegetation, soil and water (From: Lillesand and Kiefer, 1994).

The most important distinction in discussing surface albedo is between vegetated and non-vegetated surfaces. Vegetation is important because it has a relatively low reflectance in the visible part of EM spectrum and a relatively high reflectance in the near infrared (NIR) part. Non-vegetated surfaces, for example dry bare soil commonly have similar reflectances at visible and NIR wavelengths. Fig. 2.8 shows three simplified reflectance curves for dry bare soil, vegetation, and water surface as a function of wavelength. An important characteristic of the reflection by vegetation surfaces is the sharp transition in the reflection at a wavelength of about 0.7 μm. The presence of chlorophyll in vegetation leads to strong absorption at wavelengths shorter than 0.7 μm. Water, however, decreases rapidly around 0.7 μm. This is due to the strong absorption in the NIR. Compared to solid surfaces, the albedo of water surfaces has a strong dependency on the Sun's angle (see Appendix B).

2.7.3 SW Radiation behaviour in a cloudy atmosphere

It is well known that clouds play an important role in the radiation balance and in climate (Peixoto & Oort, 1992). Clouds have a strong influence on the climate of the planet by reflecting solar radiation (which cools the Earth) and trapping terrestrial radiation (which tends to warm the Earth).

However, the detailed radiative properties of clouds are not well known. They change substantially with cloud type and cloud form. The thickness of a cloud as well as the zenith angle of the Sun seems to be important factors. Inside the clouds multiple scattering dominates the behaviour of solar radiation. The absorption inside clouds occurs in drops, ice crystals, and, to a lesser extent, in water vapour for the near infrared (NIR) region of the solar EM spectrum.

Concerning these interactions, the following parameters are important for radiative transfer in a cloudy atmosphere:

- Water Cloud
- Ice Cloud
- Cloud Optical Depth
- Single and Multiple Scattering
- Absorption of radiation by cloud particles in relation to cloud microphysics
- Heterogeneous Clouds

The distinction between water and ice clouds can be interpreted on differences in radiative properties between water droplets and ice particles. These differences are listed in Table 1.

Table 1: Cloud radiative parameters for water droplets and ice particles.

	Water	*Ice*
single scattering albedo, ω	~1	0.9
scattering efficiency, Q	2.14	2
phase function, P	Mie	ray tracing

Water cloud

In general, it is assumed that water droplets are spherical, which is a robust assumption. The interaction of monochromatic light with a single spherical water particle can be described by the parameters listed in Table 1, i.e.:

1. single scattering albedo, ω
2. scattering efficiency, Q
3. phase function, P

1. Single scattering albedo

The single scattering albedo is the ratio of amount of scattering light over the total amount of light removed from the incident beam by the particle. The attenuation of the incident solar radiation is caused either by scattering or absorption. In general, it is assumed that at 0.63 μm hardly any light is absorbed by water cloud particles, so ω approximates unity.

2. Scattering efficiency

The scattering efficiency, $Q(r,\lambda)$, is the ratio of the amount of light that is scattered by a single particle, to the amount of light incident on its projected area. This coefficient depends on the radius of the sphere, r, and the incident wavelength, λ. According to Mie theory, the scattering coefficient of a perfect spherical water droplet varies strongly with its size between 0 and 4 μm. When the particles are sufficiently large the dispersion of radiation approaches a λ^{-1} dependence, leading to diffuse reflection. This explains why cloud drops and ice crystals change in direction of the incident radiation in all directions. For small particles ($r < 0.1$ μm) the cloud-radiation interaction is in the Rayleigh regime, as already mentioned. For large particles ($r > 20$ μm) the geometrical optics can be applied, which defines Q to be 2. For monodisperse water spheres of radius 0.1 to 20 μm, $Q(r)$ varies considerably with size, with mode of about 2 and maximum 4. In clouds, the size distribution is never monodisperse and therefore the variations in scattering coefficient average out. For wide distributions of particle sizes the scattering coefficient may be assumed to be 2 for large particles and about 2.3 for small ($r \approx 2$ μm) particles.

3. Phase function

As already mentioned in Section 2.6, the phase function $P(\theta)$, is the amount of energy scattered at an angle θ relative to the direction of propagation of the incident light. The angular distribution of the incident light by a single spherical water drop can be calculated exactly using Mie-theory. The angular dependency of the phase function causes different features. Fig. 2.9 illustrates the main features of phase functions for both water droplets and ice crystals. The mean features for water clouds are the distinct forward peak ($\theta = 0$), a minimum near the side-scattering angle ($\theta = 90$), the cloud bow at ($\theta = 140$), and the backscatter peak ($\theta = 180$). The cloud bow, the local maximum near 140°, is the cloud particle analogue of the rainbow. The peak near backscatter geometry, 180°, indicates the glory, which sometimes can be seen form an aircraft as a ring around its shadow.

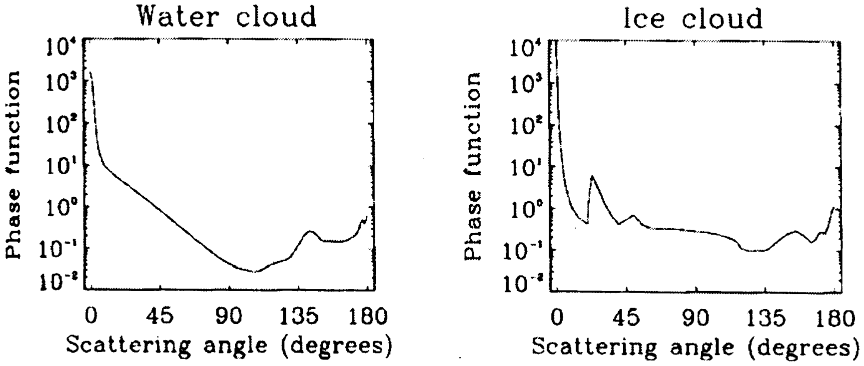

Figure 2.9: Illustration of phase functions occurring in planetary media. Shown are phase functions for: cloud droplets (left); and ice crystals (right). (From: Thomas and Stamnes, 1999)

Ice cloud

The phase function, which plays an important role in the radiative transfer in clouds, is different for ice crystals and water droplets. This is due to their different size and shape. Ice crystals occur in many shapes and sizes. The basic shapes are columns and plates, which can occur in aggregates as well. The size ranges from 10 to 2000 μm. The shape and size depend on the time the crystal has grown, the relative humidity, temperature and the history of the air mass. For large ice crystals, ($r > 100$ μm) the phase function cannot be described in an analytic formula for arbitrary shapes and sizes. Only for some non-spherical particles analytic solutions exist (Liou, 1980). However, the phase function can be obtained by ray tracing calculations. This method involves the simulation of the path of individual photons entering the crystal until it exits again or is absorbed. Repeating this for a large number of photons and recording the angles between incoming and outgoing direction, together with the fraction of photons that are absorbed, a statistical estimate of the optical properties of the crystal can be found. The accuracy of this approach depends on the validity of the assumptions made by geometrical optics. Hence, its applicability is limited to large size parameters, a criterion that is fulfilled for solar wavelengths and the ice particles found in the atmosphere.

The right part of Fig. 2.9 is showing the scattering phase function of ice clouds. Since there are differences in features of phase function between the two basic ice shapes, only general features are presented in this figure, which are the strong forward scattering at 0°, the well defined 22° halo feature, and the less defined 46° halo. Also, the cloud bow, the local maximum near 140° and the peak near backscatter geometry, 180° can be seen.

Cloud Optical Depth

In the presence of clouds, variations in the reflection and transmission properties of the atmosphere across the solar spectral region are dominated by changes in cloud optical depth, τ. Hence, the cloud optical depth is the single most important parameter for quantifying the influence of clouds on the solar radiation budget (Lenoble, 1993). It is closely related to the cloud water present within a vertical column, the liquid water path (*LWP*).

For a given effective radius r_{eff} of the cloud droplet size distribution, it is linked to the LWP with high accuracy by

$$\tau = \frac{3}{2}\frac{LWP}{r_{eff}\,\rho_{H_2O}}, \tag{2.20}$$

where ρ_{H_2O} is the density of water. For this relation, the effective radius of a cloud droplet size distribution is defined as

$$r_{eff} = \frac{\int n(r) r^3 dr}{\int n(r) r^2 dr}, \tag{2.21}$$

where n is the spectral number density of droplets. The effective radius is also the main parameter determining the cloud optical parameters required for irradiance calculations, which are given by the single scattering albedo and the asymmetry parameter. These relations provide a convenient means to incorporate cloud microphysics in radiative transfer schemes.

The cloud optical depth is as a unitless quantity defined as the product of the column density (1/cm^2) of cloud particles and extinction cross-section of a cloud particle (cm^2) (Dlhopolsky & Feijt, 2001). The latter depends on the wavelength (see Eq. 2.22). The cloud optical depth can thus be interpreted as the number of scattering events a photon would have if it was to penetrate a cloud vertically without being attenuated or deflected from the incident beam (Feijt, 2000). Excluding the effects of water vapour, the definition of the broadband cloud optical depth (τ_{BB}) is

$$\tau_{BB} = \int_{\lambda_1}^{\lambda_2}\int_0^{\infty} n(r) A(r) Q(r,\lambda)\, dr\, d\lambda = \int_{\lambda_1}^{\lambda_2}\int_0^{\infty} n(r) Q(r,\lambda)\, \pi r^2\, dr\, d\lambda, \tag{2.22}$$

where $Q(r,\lambda)$ is the scattering efficiency factor, and $n(r)$ is the number of particles of radius r. The first integral is over the cloud droplet radius r. The second integral is over the wavelength. Evaluation of Eq. (2.22) requires knowledge of both the cloud droplet distribution and the scattering efficiency factor Q (see Hansen & Travis, 1974).

The most important effect of changing the optical depth of a cloud layer is that it changes the amount of reflected radiation and thereby alters the energy reaching the Earth's surface and the atmosphere below a cloud layer (Cotton & Anthes, 1989). This is caused by the redirections of photons after interaction with a water droplet in a cloud. Because absorption is low, a photon may scatter 100 times on its path through the cloud. The photon may travel a considerable distance through the atmosphere, before being scattered outside the cloud either to the surface or into space. This multiple scattering induces effects that are specific for clouds. The increase of the optical path may amplify weak atmospheric absorption or scattering.

Single and multiple scattering

Light scattering in planetary atmospheres is usually divided into two parts: single scattering by small volume elements in the atmosphere and multiple scattering by the entire atmosphere (Hansen & Travis, 1974). This division requires that the scattering particles be sufficiently separated that they may be treated as independent scatterers, a condition which is met in planetary atmospheres.

Consider the illumination of the atmosphere by the Sun. Assume that the particles are well separated; so that each is subjected to direct solar radiation. A small portion of the direct radiation incident on the particle will be scattered and thereby gives rise to scattered or diffuse radiation (see Fig. 2.5). If the diffuse radiation arriving from all parts of the medium is negligible compared with the direct radiation, the medium is said to be *optically thin* and diffuse radiation is unimportant. If we were to double the number of scatterers in an optically thin medium, the scattered or diffuse radiation would also be doubled. However, it often happens that the diffuse radiation itself is an important additional source of radiation, becoming a source for still more scattering, etc.

The diffuse radiation arising from scattering of the direct solar beam is called *first-order* or *single* scattering. If additional radiation events need to be included, the radiation is said to be *multiple scattered*, and the medium in which this is important is said to be *optically thick*. Thus, in many situations of interest in planetary media, the radiation field is not only determined by the transmitted incident radiation field but also by the "self-illumination" from the medium itself (Thomas & Stamnes, 1999). This latter is especially important in cloud-cloud interactions.

A large part of the scattered radiation is scattered into backward hemisphere. Clouds have therefore a considerable impact on decreasing solar energy reaching the ground. A single cloud droplet scatters more radiation in the forward direction then in the backward direction. This principle of forward and backward scattering is important in clouds, since more scattering events will induce a higher chance for a cloud particle to absorb radiation.

Absorption of radiation by cloud particles in relation to cloud microphysics

The optical thickness, single scattering albedo, and phase function of the cloud, as well as the reflectance of the underlying surface and the water vapour distribution of the environment in which the cloud is located govern the absorption of solar radiation by clouds. Theoretical calculations suggest that water clouds absorb 15–20% of the incident solar radiation, with the largest values arising from the thickest clouds having large cloud droplets, an overhead Sun, and little water vapour above the cloud.

Several investigators have estimated that precipitation-sized drops can appreciably increase cloud absorptance (Manton, 1980; Welch *et al.*, 1980; Wiscombe *et al.*, 1984 in Cotton & Anthes, 1989). Because precipitation-sized drops form by collecting smaller cloud drops, they typically represent a miniscule percentage of the total drop concentration. Drizzle-sized drops have a concentration usually not exceeding 100 droplets per m^3, compared to cloud droplet concentrations of the order of 10^8 to 10^9 droplets per m^3.

Welch *et al.* (1980) noted that if the liquid water in the tops of middle and high clouds is distributed mainly in larger drops (or ice particles) rather than on small cloud droplets, 10-23% reduction in cloud albedo (reflectance) can occur. Thus the facts that large drops exhibit very low reflectance and that they grow at the expense of cloud droplets suggest that the magnitude of cloud and planetary albedo is sensitive to the relative abundance of precipitation-sized particles in the upper levels of clouds (Cotton & Anthes, 1989).

Heterogeneous clouds

Radiative transfer calculations often use a 1D column model of the atmosphere containing a plane-parallel, homogeneous (PPH) cloud.

Since cloud fields are often broken (Boers *et al.*, 2000), biases arise when a cloud structure tends to be inhomogeneous. A horizontal discontinuous cloud layer often means variations in the vertical as well. These variations in the vertical extent of clouds cause 3D cloud-radiation effects like shadows (Feijt, 2000). Also sides of clouds cause biases in radiation measurements. Since the sides of the clouds interact with the radiation reflected from the surface, the cloud-surface interaction on finite cloud fields will be different from that in a plane-parallel cloud (Kobayashi, 1989).

There have been some sensitivity studies on the impact of 3D effects on radiative transfer. A method, which is widely used, is Monte Carlo modelling, which calculates the path of large number of photons (typically a million) through a cloud. Each individual scattering event is taken into account. The major advantage of the Monte Carlo method is the ease with which it can be applied to many complicated problems, particularly to non-parallel atmospheres. Other bias sensitivities in radiative transfer calculations assuming PPH are mixed phase clouds (i.e. a cloud containing both water droplets and ice particles) and multi layered clouds. Since ice crystals and water droplets act differently on (shortwave) radiation, biases arise when a cloud is assumed to be or in water or in ice phase.

3. Measurements and Methods

This chapter is introducing retrieval methods for deriving downwelling solar surface irradiance from satellite measurements. Since satellites play an increasing role in climate research in the last decades, their (retrieved) products need to be evaluated with independent data to establish their accuracy and identify possible shortcomings.

In the next section, the instruments used to measure reflected and transmitted solar radiation are introduced. Then, a summary of the retrieval method is given that uses the measurements to retrieve cloud optical depths. The latter is an important parameter for quantifying the influence of clouds on the radiative transfer model (RTM). Also details on the retrieval technique applied to the measurements are given.

Finally, an introduction of the AVHRR analyse environment KLAROS is introduced. In this thesis, KLAROS is used to get a better understanding of the behaviour of the atmospheric radiative processes specified for the selected case studies, which are presented in the following chapter.

3.1 Measuring Instrumentation

For the retrieval of cloud optical depths from reflected and transmitted solar radiation, satellite data of the 0.63 μm bi-directional reflection obtained by the AVHRR instrument flown onboard the NOAA-14 satellite are used together with simultaneous and collocated measurements of the global downwelling solar irradiance as obtained from ground-based pyranometers.

3.1.1 AVHRR

The AVHRR instrument is an imaging radiometer onboard the NOAA series of polar-orbiting, Sun-synchronous satellites, which fly at a height of approximately 850 kilometres. The AVHRR infers the radiance within five spectral bands centered at 0.63, 0.9, 3.7, 10.8 and 11.9 μm. The main characteristics of these spectral bands are described below. Its scan mirror rotates at sixty revolutions per second, acquiring 2048 samples with a viewing angle of ±55 degrees and an instantaneous field of view of 0.7×10^{-3} degrees. This results in a nadir pixel resolution of 1.1 x 1.1 km, and increases up to about 1.1 x 2.5 km at 55 degrees. Photo diodes made of silicon are used as detectors for the visible channels and have radiometric resolution of 10 bits. They are sensitive to the incident radiance as filtered by the spectral response function for the visible channels.

The 0.63 μm channel is mainly used for the identification of clouds, because at this wavelength both land and sea surface are dark and clouds are bright. The main contributions from other atmospheric constituents (gases, aerosols, clouds) are due to Rayleigh scattering, ozone and aerosols. Since this wavelength band is centered near the peak of the solar spectral curve (see Fig. 2.2), it measures a relatively high signal. Noise factors (e.g. Rayleigh scattering) are relatively low in this channel. Therefore, this channel has a high signal to noise (S/N) ratio. This ratio must be kept large, in order to maintain high image quality.

The 0.9 μm channel is sometimes used to obtain cloud properties over sea, because the sea is dark and Rayleigh scattering can be neglected. However, there are absorption bands of oxygen and water vapour in this wavelength band. Therefore, the S/N ratio is lower than the S/N of Channel 1. The combination of 0.63 and 0.9 μm channels is most frequently used to estimate the amount of vegetation. This is due to the different absorption characteristics of vegetation in both spectral bands.

The 3.7 μm channel measures radiance both from reflected sunlight and from thermal emission. However, this channel is receiving relatively low radiance, since it is centered between the two radiative spectral curves from both Earth and Sun (see Fig. 2.2). Hence, the signal to noise ratio is low. If the solar contribution can be isolated, the difference with the 0.63 and 0.9 μm channels can be used to estimate droplet size for water clouds. In cloud free conditions snow can be identified. During the night low stratus and fog can be identified from the difference in emissivity at 3.7 and 10.8 μm. The 10.8 μm channel is most appropriate to estimate the temperature of clouds and surface, since it is located in the middle of the atmospheric window and thus atmospheric absorption is at a minimum, but not negligible.

The 11.9 μm channel is mainly used to estimate the atmospheric absorption in the 10.8 μm channel. At 11.9 μm the atmospheric absorption is higher due to a water vapour band and CO_2. Therefore, the atmospheric absorption in the 10.8 μm channel can be estimated from the difference of measured radiance with the 11.9 μm signal. This method is widely employed to retrieve sea surface temperatures. This method is not very effective to retrieve land surface temperatures, because the emissivity of land surface at 10.8 and 11.9 μm are different and depend on surface type and vegetation.

Instruments measuring radiation show a significant wavelength-dependence in their sensitivity. This dependence is described by the spectral response function of an instrument. For the NOAA spectral channels described above, spectral response functions are measured as well. These response functions are optimised to measure cloud and surface characteristics with minimum of contamination from other atmospheric constituents. The spectral response functions of channel 1 and 2 of the AVHRR instrument are given in Fig. 3.1. More information about the AVHRR instrument can be found in the NOAA Polar Orbiter User's Guide (Kidwell, 1998).

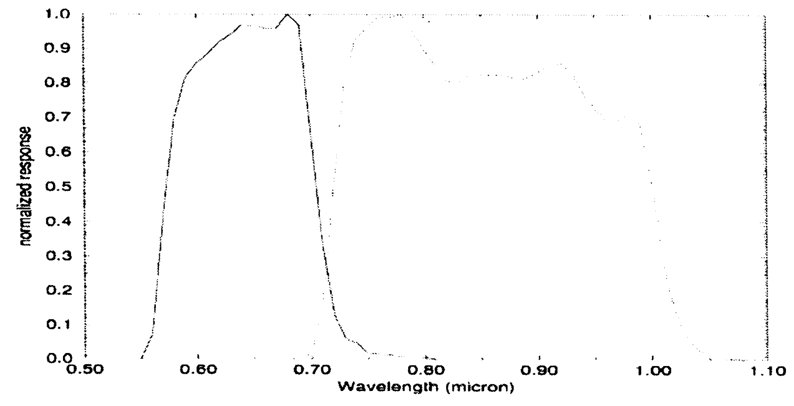

Figure 3.1: Spectral response function of the 0.63 μm channel (solid line) and the 0.9 μm channel (dashed line) of the AVHRR instrument on board NOAA-14.

Measurement accuracy

The accuracy of AVHRR measurements is mainly determined by the accuracy of the calibration (Deneke, 2002). The spectral response function of the instrument is measured before launch. There is no on-board calibration of the visible channels. Due to the lack of a stable onboard calibration source for the visible channels, the accuracy of calibration of the AVHRR is rather limited. In case of the instrument onboard NOAA-14, part of the problem is probably amplified by rapid non-linear changes in the sensitivity of the sensor shortly after its launch and after the year 1998 (Deneke, 2002). Changes in sensitivity are mainly caused by cosmic radiation. This latter significantly reduces the sensitivity of the instrument over the lifespan of the satellite. Deneke (2002) assumes the overall accuracy of the calibration to be in the order of 5%.

3.1.2 Pyranometer

The KNMI maintains an operational network of 32 stations in The Netherlands, measuring the global broadband solar irradiance at the surface with pyranometers. The geographical distribution of the KNMI stations containing a pyranometer together with additional information on these stations can be found in Appendix C.

Secondary standard pyranometers of type CM 11 (see Fig. 3.3) built by Kipp en Zonen are used for the measurement of global solar irradiance at KNMI's meteorological stations. Dataloggers record the mean, minimum and maximum values of irradiance measured by the instruments during 10-minute intervals.

The thermoelectric pyranometer is an instrument capable of an accurate measurement of broadband hemispherical irradiances in the solar spectral region. Its main application is the measurement of the downwelling solar irradiance. It can measure either the global or the diffuse irradiance. For the latter, the pyranometer is operated in shaded conditions, where a shadow disk blocks the direct beam of the Sun.

The pyranometer's operational principle is based on the effect of differential heating of an absorbing detector exposed to shortwave radiation, relative to a heat sink whose thermal state its not altered by radiation. The resulting temperature difference is used to infer the level of incident irradiance. In case of the CM 11, a black painted ceramic disk is located in the center of the instrument and acts as absorber. A schematic view of the pyranometer's device is shown in Fig. 3.4.

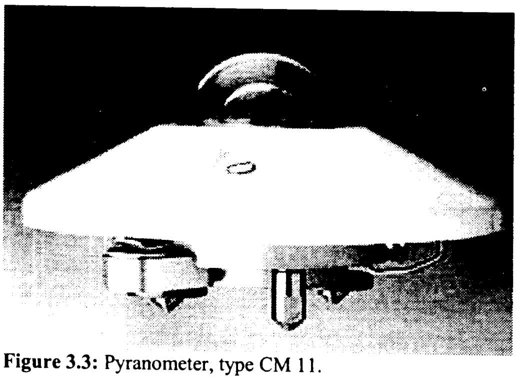

Figure 3.3: Pyranometer, type CM 11.

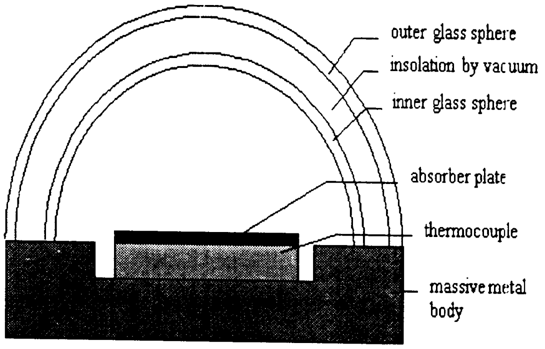

Figure 3.4: Schematic view of the pyranometer's measuring device.

The disk is in good thermal contact with the pyranometer body, which serves as the heat sink. 100 thermocouples produce a voltage proportional to the temperature gradient from the center of the disk to the instrument's body. They are applied in thin-film technique and are arranged in a rotationally symmetric manner, to minimize differences in the directional sensitivity. Two hemispherical glass domes filter out longwave radiation and shield the instrument from environmental influences. They transmit radiation in the spectral range from 0.3 to 2.8 μm. The remaining part of the solar irradiance is absorbed and heats the glass dome.

Measurement accuracy

Several parameters influence the accuracy of a measured dataset, such as the thermal offset, the length of the measurement period, the maintenance and the number of instruments. Each instrument is calibrated biannually, thereby replacing the instrument installed at a particular site. These operating conditions are less than optimal and can affect the reliability of the dataset (Deneke, 2002). As the instruments are operated automatically without ventilation and heating and checked at rather long maintenance intervals of up to a year, the accuracy of the measurements is probably somewhat degraded by pollution of the instrument's glass dome, but is found to not exceed 5% (Kuik in Deneke, 2002). A thorough research on instrumental biases is beyond the scope of this study. An accuracy of the pyranometer to be within ± 5% is assumed (Deneke, personal communication).

3.2 Deriving Downwelling Solar Irradiance Fluxes at the Surface

The method of Deneke (2002) of deriving downwelling solar surface irradiance (DSSI) fluxes is based on classical electrodynamics, and applies Maxwell's equations to the interaction of radiation with the Earth's atmosphere. Maxwell's equations are the set of four fundamental equations governing electromagnetism (i.e. the behaviour of electric and magnetic fields). However, it is beyond the scope of this study to explain these equations in full detail. This theory provides the tools for calculating the radiation field. These tools are being used as building blocks for the satellite retrieval scheme.

Paragraph 3.2.2 will introduce the retrieval output, i.e. cloud optical depth. Further, the assumptions made for an atmospheric state are given. A detailed radiative transfer code, which is based on mean conditions of both atmosphere and cloud, is used to calculate reflectivities. These reflectivities are stored in a lookup table (LUT). The LUT and the technique used to infer the retrieval output from this LUT are given in paragraph 3.2.4 and 3.2.5. The AVHRR analyse environment KLAROS is introduced in Section 3.3.

First, the retrieval input parameters obtained from radiance and irradiance measurements are introduced. Both the radiance and irradiance values have been renormalized to mean Sun-Earth distance and converted to bi-directional reflectance and broadband atmospheric transmissivity, respectively.

3.2.1 Retrieval input

Bi-directional reflectance

Since the Earth is partly reflecting solar radiation into space, the AVHRR is detecting this reflected radiance in two visible spectral bands.

The 0.63 μm channel, channel 1, is mainly used to obtain cloud optical depths, because this wavelength has a high contrast between clouds and surface. Channel 2 may be used to obtain cloud properties over sea, because the sea is dark and Rayleigh scattering can be neglected. However, there are absorption bands of oxygen and water vapour in this wavelength band that disturbs the observed cloud radiance. Hence, the spectral range of the 0.63 μm channel has been selected for quantitative analysis to minimize the influence of the atmosphere and simplify the retrieval of cloud and surface properties.

Since the satellite retrieval uses bi-directional reflectance values as input, radiance measurements in channel 1 from the AVHRR instrument have to be converted. Therefore, the following general mathematical construction is being applied

$$r_i \equiv \pi \frac{I_i}{\mu_0 S} = \pi \frac{\overline{I_i} \Delta_i}{\mu_0 S}, \tag{3.1}$$

where r_i is the bi-directional reflectance at the TOA and $\overline{I_i}$ is the mean spectral radiance for a given channel, where the index i indicates the channel number. The conversion is assumed to be a linear function of the received radiance. The ratio in Eq. 3.1 represents the measured radiance to the one expected for a perfectly reflecting Lambertian surface without atmospheric attenuation.

Broadband Atmospheric Transmissivity

Pyranometers are measuring broadband global solar irradiances at the surface. However, instead of using absolute values of global irradiance, the atmospheric transmissivity is being used as input parameter to the pyranometer retrieval. This is done in order to facilitate the comparison of the results obtained at different solar zenith angles, as the variability caused by changes of the incident TOA irradiance is removed. The parameter, which is further referred to as Broadband Atmospheric Transmissivity (BAT), is defined as

$$T \equiv \frac{F_{glob}}{\mu_0 S}, \tag{3.2}$$

where F_{glob} is the global irradiance measured at the surface and S is the solar constant, both in W m^{-2}.

3.2.2 Retrieval output

The output of both pyranometer and satellite retrieval is the cloud optical depth. The cloud optical depth is being used as a linking parameter between satellite and ground based measurements because of its unique relation to both measured radiative quantities. As an example, the relation between the reflectivity and cloud optical depth is shown in Fig. 3.5. The relation of the transmissivity to the cloud optical depth is inversely proportional to the plot shown in this figure. This means that low cloud optical depths are corresponding with high transmissivity values, and vice versa.

Further, Fig. 3.5 shows that *small* changes in the lower or higher end of the curve can cause *large* differences in cloud optical depths. Therefore, a proper error analysis of the instrument calibration is an important requirement to assess error propagation that contributes to the bias of the retrieval output.

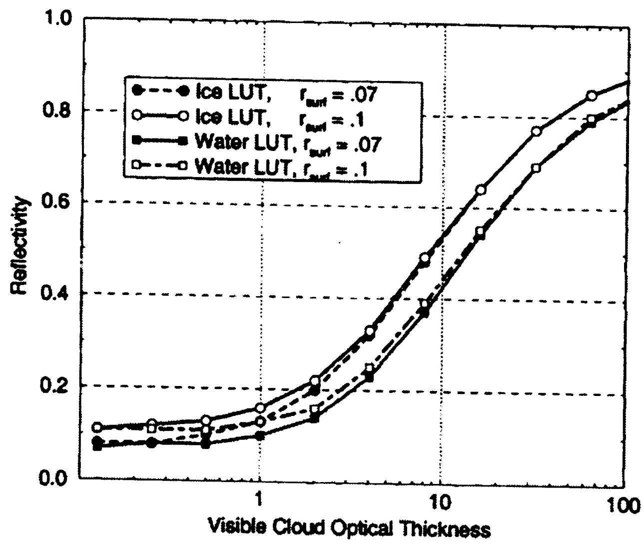

Figure 3.5: Example of ice and water LUTs, using cloud optical depth as a function of reflectivity (From: Dlholpolsky & Feijt, 2001).

To retrieve cloud optical depths from the measured quantities, a detailed radiative transfer code has been used. This code uses an atmospheric model, based on mean atmospheric conditions for its radiative transfer calculations. However, to model the atmosphere accurately, many assumptions have to be made. The following section is introducing most of the assumptions, which are implemented in the RTM.

3.2.3 Assumptions on Atmospheric State

The atmosphere is represented by the mid-latitude summer profile of Anderson *et al.* (1986). However, the mean vertically integrated water vapour (IWV[1]) column is adjusted to 16.4 kg/ m^2 and the ozone column to 328 DU, which are the climatological mean values for De Bilt, the Netherlands (52.10° N, 5.17° E). An aerosol profile with an optical depth of 0.1925 at 0.55 μm and of water-soluble composition is included in the atmosphere. To incorporate the effect of clouds in this atmosphere, a representative water cloud or an ice cloud is assumed (chosen *a priori*).

The water cloud droplet size spectrum is given by a Gamma-shaped distribution with an effective radius of 10 μm and an effective variance of 0.1. This choice of droplet spectrum is consistent with the ISCCP retrievals (Deneke, 2002). The optical properties of the cloud are calculated according to Mie theory. The cloud base and top altitudes are fixed to 1 and 2 km in the atmosphere, and vertically homogeneous profiles of the cloud optical properties are assumed.

---

[1] The IWV is a measure for the total amount of water vapour present in an atmospheric column and accounts for most of the variability in columns-integrated atmospheric absorption by water vapour (Li according to Deneke, 2002).

For the location of the ice cloud, the height interval from 8 to 9 km is chosen. Compared to water clouds, much more uncertainty exists in the optical properties of ice particles, which are caused by the large variety of crystal shapes found under typical atmospheric conditions. The optical properties of the C2 model (see Hess & Wiegner, 1994) consisting of imperfect hexagonal ice crystals and obtained by ray tracing calculations are used.

A realistic estimate of the surface albedo is an important prerequisite for an accurate retrieval of cloud optical depth from reflected and transmitted solar radiation. The dominating land cover throughout the Netherlands, and in particular at the measurement stations, are grass pastures and low vegetation. For grassland within the 0.63 μm spectral region and the total solar spectrum, typical values of 10% and 18% are reported in the literature, respectively (Deneke, 2002). Effects resulting from spectral dependence and bi-directionality of the surface albedo are not taking into account.

DISORT Method

The assumptions made for a mean atmospheric state are used for doing radiative transfer calculations. An RTM carries out these calculations. The RTM, applied by Deneke (2002), uses the Discrete Ordinate Method (DISORT) for the radiative transfer calculations.

The DISORT method has been development by Chandrasekhar (1960) for application to the transfer of radiation in planetary atmospheres. Liou (1973) demonstrated that the DISORT method is a useful and powerful method for the computation of radiation fields in aerosol and cloudy atmospheres. The method involves the discretization of the basic radiative transfer equation and the solution of a set of first-order differential equations. With the advance in numerical techniques for solving differential equations, the DISORT method has been found to be efficient and accurate for calculations of scattered intensities and fluxes (Liou, 2002). Further, DISORT is a code written in FORTRAN and applies to vertically inhomogeneous, nonisothermal, plane-parallel media and it includes all the physical processes discussed previously, namely thermal emission, scattering, absorption, and bi-directional reflection (Thomas & Stamnes, 1999).

The radiative transfer calculations are used as basis for the satellite and pyranometer retrieval. The output of these calculations, which are 0.63 μm bi-directional reflectances and BAT, are stored in lookup tables (LUTs).

3.2.4 Generation of Lookup tables

In order to make both pyranometer and satellite retrieval ready for implementation, RTM calculations are needed to generate the LUTs for various viewing geometries and cloud optical depths. These LUTs are required to relate AVHRR Ch 1 bi-directional reflectivities and pyranometer BAT to cloud optical depths. The generation of the LUTs is a computer intensive job.

To generate the LUTs, radiative transfer calculations have been conducted at equidistant values of the cosine of the solar zenith angle (0.1-1.0 in steps of 0.05). At each value of the solar zenith angle, 14 values of the cloud optical depth are used ranging from 0.125 to 512 and spaced at integer powers of 2. For the satellite retrieval, radiances have been output at 19 values of the relative azimuth (0-180° in steps of 10°) and the cosine of the satellite zenith angle (0.4-1.0 in steps of 0.05). Examples of LUTs are illustrated in Fig. 3.5.

As for the pyranometer retrieval, three sets of lookup tables are generated, based on values of the mean integrated water vapour (IWV) and its standard deviation (8.9, 16.4 and 23.9 kg/ m^2). These actual IWV values are obtained from the radiosonde soundings conducted at De Bilt at six-hour intervals. The reason for using three sets of LUTs is because the BAT is significantly influenced by the vertically IWV due to strong absorption lines in the NIR of the solar EM spectrum (Deneke, 2002).

For the model inversion, the function linking cloud optical depth and the reflectance/ transmissivity is obtained by multi-linear interpolation in the parameters describing the geometrical setup of satellite, Sun and the pyranometer (see Fig. 2.3). As a smooth function linking the cloud optical depth and reflectance is expected, bicubic spline interpolation is used to determine the cloud optical depth corresponding to a given measurement.

3.2.5 Retrieval Technique

Once the LUTs are available, retrievals are used to obtain cloud optical depths from TOA bi-directional reflectances and BAT. The same technique is used for both pyranometer and satellite retrieval. Therefore, the satellite retrieval has been chosen to outline the retrieval technique.

The basic idea of the satellite retrieval is to match the reflectivity value measured by the satellite with the reflectivity produced by the RTM under the same Sun-satellite geometry. For a single satellite pixel, multi-linear interpolation in the geometrical parameters and the vertically IWV is used first to extract the reflectivity for a given measurement at all values of cloud optical depth included in the LUTs. The thus obtained pre-calculated reflectivities are compared with the measured reflectivity for each pixel to obtain a cloud optical depth. The modelled cloud optical depth is assumed to be the best estimate of the actual cloud optical depth. However, results exceeding a cloud optical depth above 80 and 50 for water and ice clouds, respectively, in any one of the two retrievals are rejected. The retrieval functions become too sensitive to instrumental and modelling errors at larger values of the optical depth for reliable results (Deneke, 2002).

For comparison with pyranometer retrieved *broadband* cloud optical depths, the obtained satellite retrieved *narrowband* cloud optical depths have to be converted to broadband cloud optical depths. This conversion is being conducted with Eq. 2.20. It is important to mention that applying this equation, further assumptions have to be made on atmospheric state, since atmospheric absorption characteristics becomes more important. To obtain satellite retrieved DSSI values; first the pyranometer LUT is used to obtain transmissivity values from calculated broadband satellite cloud optical depths, using interpolation technique described in paragraph 3.2.4. Hence, Eq. 2.7 is being applied to calculate DSSI values.

3.3 KLAROS

The AVHRR analysis environment is called KLAROS, which stands for 'KNMI Local implementation of APOLLO Retrievals in an Operating System' (Dlhopolosky & Feijt, 2001). The structure and operation of the KLAROS environment is illustrated in Appendix D. KLAROS is written in C programming language and can be run operationally at the command line or from within an image processing environment, such as IDL (Interactive Data Language).

KLAROS a two-step approach. In step one; pixels are identified as cloud-free or cloud-filled. The cloud detection part consists of tests, using AVHRR spectral channels. These tests are adopted from the AVHRR Processing Over Land cloud and Ocean (APOLLO), which was developed in the 1980's (Saunders & Kriebel, 1988). Cloud detection is described in detail in paragraph 3.3.1. In the second step, the radiances of cloudy pixels are interpreted in terms of cloud parameters, which are described in paragraph 3.3.2.

3.3.1 Cloud Detection

Cloud masking typically applies to the procedure of characterizing a pixel as being cloud-free or cloud-filled. The APOLLO scheme is a supervised method described by Saunders and Kriebel (1988). The scheme consists of five daytime or five nighttime tests applied to each individual pixel to determine whether that pixel is cloud-free, partly cloudy or cloud-filled. The pixel is only identified as cloud-free or cloud-filled if it passes all the tests to identify that condition, otherwise it is assumed to be partly cloudy.

Threshold Database

Historically, clouds are detected by comparing reflectivity and temperature measurements with the expected values for cloud free conditions. These values are determined in several different ways. Frequency histograms of measurements are the simplest. It is necessary to find the darkest reflectivity pixel and the warmest temperature pixel. This method, however, requires that there be a clear sky pixel within the area of observation. An underlying assumption is that the reflectivity and temperature for the clear sky area is indeed the same for a large area beneath a cloud deck. Surfaces with highly variable reflective properties increase the spread of the histogram and make this analysis cumbersome.

Variability due to spatial topography, water, rivers, and sub-pixel water masses have been shown to frequently confound this technique.

The histogram method is time consuming and in many cases cannot make an accurate threshold without human interaction. The KLAROS environment was designed to work with the use of thresholds. These thresholds operate on a pixel-by-pixel basis and are much faster and therefore appropriate for an operational environment. The temperature database is derived from the HIRLAM NWP model. The reflectivity database has been created from two years of NOAA-14 AVHRR data clear skies and verified with synoptic observations.

Clear Sky Threshold

Relatively high reflectivities in the visible and relatively low temperatures in the IR are the standard deciding factors for a cloudy area. The thresholds for the APOLLO cloud mask scheme were based on histogram analysis of AVHRR images at middle latitude over Europe and the North Atlantic. Histogram analysis depends on there being a strong peak, which distinguishes a cloud field from the underlying surface. In general, this must be applied to each image because other images will have different surface properties, viewing geometries, and cloud fields.

Thresholds of reflectivity must take into account the fact that scenes can consist of several surfaces, all of which can have different reflection characteristics. Also, the same surface will not have the same reflectivity if it is observed from a different viewing angle and time of day, due to anisotropy. For an overcast cloud pixel, the reflectivity will be larger than if it was observed at other angles, excluding the backscattering angle where there is also large anisotropy. Therefore an ideal reflectivity database will have categories based on surface type, vegetation type, and viewing angle of satellite.

The temperature thresholds should be dependent on the time of day, due to surface warming by the Sun. This warming will depend on how much solar radiation reaches the surface and how much is actually absorbed. There is also a dependence on viewing geometry due to absorbing gases in the IR along the path of observation through the atmosphere. Most important is that histogram analysis requires that there be at least some clear sky within the area being analysed. This area needs to be homogeneous to the extent that the clear area can be used for determining the surface temperature and reflectivity beneath the cloudy pixels. The problem is compounded by multi-layered cloud systems where the radiating surface under the satellite observed cloud is another cloud.

Cloud Threshold

Cloudy scenes are identified with a threshold method, which tests if the signal in a channel or combination of channels originates from the surface in a cloud free atmosphere. If not, the scene is assumed to be cloud contaminated. Here, the main tests for daytime are presented. A scene is identified cloudy if one of the following conditions is met:

Temperature test:

$$T_{10.8\mu m}\text{ (measured)} < T_{10.8\mu m}\text{ (cloud free)} - \text{temperature\_threshold}$$

Reflectivity test:

$$R_{0.6\mu m}\text{ (measured)} > R_{0.6\mu m}\text{ (cloud free)} + \text{reflectivity\_threshold}$$

Semi-transparency test:

$$T_{10.8\mu m}\text{ (measured)} - T_{11.9\mu m}\text{ (measured)} > T_{10.8\mu m}\text{ (cloud free)} - T_{11.9\mu m}\text{ (cloud free)} + \text{semi-transparency\_threshold}$$

T_λ is the equivalent black body temperature in the spectral channel denoted by λ. R_λ is the reflectivity in the spectral channel denoted by λ (Feijt, 2000).

The temperature test requires an estimate of the surface temperature for cloud free conditions. In this aspect APOLLO and KLAROS differ. In KLAROS, the surface temperatures originate from an operational numerical weather prediction model called HIRLAM, the 'HIgh Resolution Limited Area Model', whereas in APOLLO histogram analysis over large areas from the satellite overpass under study is used.

HIRLAM surface temperatures are used for the temperature threshold and are available for every three hours. In KLAROS, a map of HIRLAM surface temperatures is made for each satellite overpass, adequately defining the surface temperature beneath the clouds. An advantage of this data set is that it automatically adjusts for seasonal changes of surface temperature and changes due to short-term changes in air mass.

The reflectivity test requires an estimate of the reflectivity for cloud free conditions. In APOLLO this value is also obtained from histogram analysis. In KLAROS the surface reflectivity is estimated from a combination of three sources:

1. Histogram analysis of the satellite observations under study
2. Histogram analysis of a recent satellite observation at clear sky
3. A two year data set of AVHRR radiances collocated with synoptic observations of clear sky

The semi-transparency test is based on the difference in absorption and scattering properties of water droplets and ice crystals at 10.8 and 11.9 µm. This results in different optical thicknesses and thus different cloud emissivities and equivalent black body temperatures. Minimum differences occur for cloud free conditions and for opaque clouds, when emissivity in both channels is near unity. The maximum difference is governed by the microphysical properties of the cloud and the cloud top and surface temperature. The difference is largest for small water spheres and decreases with increasing drop size. The test is sometimes referred to as cirrus-test, because it is most effective in case of a large temperature difference between surface and cloud, i.e. in case of cirrus.

Thus, the presence of clouds within a pixel affects the radiances measured by all the AVHRR channels. This effect has been studied and various combinations of radiances have been used to refine the cloud detection procedure, as mentioned above. Other useful combinations of AVHRR channels to identify cloudy pixels are:

- Ratio Channel 2 / Channel 1

As Channel 1 and 2 are used as primary cloud detectors (see paragraph 3.1.1), the ratio of Ch 2 to Ch 1 is used as a secondary cloud detector. The importance of this ratio is due to the fact that the vegetative surface features will not appear in the signal if a cloud is within the field of view. Therefore, the difference between Channel 1 and 2 will be very small.

- Temperature difference Channel 4 - Channel 3

This temperature test is mostly used at nighttime. At daytime the radiance measured in AVHRR channel 3 is influenced by scattered solar radiation and emitted radiation. Thus, to calculate possible temperature differences between both AVHRR channels, the reflected component has to be removed. This is done at nighttime.

The temperature difference Ch 4 – Ch 3 is strongly dependent on the presence of a cloud. This is due to the different absorption characteristics of water of both channels and also the temperature dependence of the Planck function. The importance of the Ch 4 – Ch 3 is in its ability to distinguish cloud from surface when the cloud top temperatures are close to the temperature of the surface and there is no visible channel information to help detect them.

- Temperature difference Channel 3 - Channel 5

The difference Ch 3 – Ch 5 is intended to help detect medium and high level clouds. The difference is due primarily to the dependence on the temperature distribution of the Planck function. The difference can be useful in separating different cloud fields. The variation of the Planck function within the 3.7µm wavelength range of Ch 3 is T^6, whereas that in the 11.9 µm range of Ch 5 is T^2. This magnifies the effect of the different radiating surfaces within the field of view.

3.3.2 Cloud properties

KLAROS includes retrievals of the following cloud parameters:

- Visible Optical Depth
- IR Emissivity and Cloud Top Temperature
- Cloud Water Content
- Effective Particle Radius

Only the visible optical depth $\tau_{0.63\mu m}$, IR emissivity and cloud top temperature are relevant for this study and are described below.

Visible Optical Depth
The $\tau_{0.63\mu m}$ is retrieved from the reflectivity $R_{0.63\mu m}$. The surface reflectivity is estimated in a similar way as for cloud detection. The database of doubling-adding (DAK) calculations of reflectivity is searched for the appropriate Sun-satellite geometry, cloud type, and surface reflectivity. This results in 12 values of $R_{0.63\mu m}$, corresponding to 12 values of the optical depth. The thus obtained pre-calculated values are compared with the measured reflectivity for each pixel to obtain an estimate of optical depth at 0.63 μm.

IR Emissivity and Cloud Top Temperature
The IR absorption optical depths in this scheme is defined as half the visible optical depth:

$$\tau_{ir} = \tau_{vis}/2. \tag{3.3}$$

This value is a reasonable approximation (Minnis in Dlhopolsky & Feijt, 2001). It is used to calculate the emissivity of the clouds being observed and is defined in the following equation:

$$\varepsilon = 1 - e^{\tau_{ir}/\cos\theta}, \tag{3.4}$$

where θ is the viewing zenith angle. For optically thick clouds, the emissivity will be that of the cloud and equal to 1. For optically thin clouds, however, there is radiation transmitted through the cloud from the surface and underlying atmosphere (or cloud). In the KLAROS environment, the surface radiation is estimated from the surface temperature supplied by the HIRLAM surface temperatures. TOA radiance, $I_{10.8\mu m}$, is calculated from the 10.8 μm channel of AVHRR. If this measured radiance is less than the radiance from the surface, $I_{surface}$, it is assumed that the difference is due to the presence of a cloud. We apply the following formula to separate the cloud radiance, I_{cloud}, from the measured signal:

$$I_{10.8\mu m} = (\varepsilon)I_{cloud} - (1-\varepsilon)I_{surface}. \tag{3.5}$$

The cloud top temperature, *CTT* is now related to I_{cloud} by the Planck function and the spectral response function of the instrument.

4. Case Studies

In this chapter, three case studies are presented which are based on data from ground-based pyranometers and the NOAA-14 AVHRR instrument. Cases are selected on their cloud cover fraction. The selection procedure has been executed on synoptic observational data. Furthermore, KLAROS is used to visualize and analyse each case as an extra consistency check of the synoptical situation. A justification of the three cases is presented below.

1. *Clear Sky*

A clear-sky case is chosen to act as a reference case. This is because clear sky observations provide the most reliable reference cases for analysing the representation of aerosols and gaseous absorption in RTMs, as the variability of cloud properties introduces large uncertainties in the modelling of cloudy atmosphere (Deneke, 2002). Clear-sky conditions are therefore often used as reference for an assessment of the effect of clouds on radiation. Cloud cover fractions of 0 oktas are used as a selection criterion for this case.

2. *Overcast*

To analyse the effects of clouds on the output of both pyranometer and satellite retrieval, overcast cases are selected on cloud cover fractions of 8 oktas. This type of cloud appears to be homogenous over a large area. This has two advantages:

1. Collocation of satellite and ground-based observations is less sensitive.
2. The cloud field resembles to a high extent a homogenous plane-parallel (PPH) single cloud layer, which is assumed in the RTM.

To analyse the impact of precipitation on pyranometer measurements as well, overcast scenes have further been screened on their synoptic precipitation records. Hence, two sub-cases are selected. For one overcast situation, no precipitation has been recorded, while the second case did report precipitation.

3. *Broken Clouds*

In the third case study, the effect of broken clouds on pyranometer measurements and the satellite retrieval is analysed. Inhomogeneous clouds are very difficult to model with respect to radiative properties, because of their morphology. Also, this type of clouds is more sensitive for collocation errors than PPH clouds. The collocation principle is further outlined in Section 4.1.

Reported cloud cover fractions of 3 to 5 oktas are used to select a broken cloud case. It should be noted that stratus also could produce these amount of cloud cover fractions. Therefore, KLAROS is used to overcome this problem.

The information on the geolocation of the satellite is important for comparison with ground-based measurement. Table 2 is showing the relevant satellite (geometrical) information for each case study.

Table 2: Information on relevant measurement geometry for each single case study.

	Clear Sky	*Overcast* *(no precipitation)*	*Overcast* *(precipitation)*	*Broken Cloud*
Date (DOY[2])	28 July 1999 (209)	2 May 2000 (123)	22 July 1999 (203)	24 June 1999 (175)
NOAA-14 overpass time in UTC	14:32	15:09	13:59	14:13
solar zenith angle, θ_0	46°	56°	41°	41°
satellite zenith angle, θ_s	19°	21°	20°	4°
relative azimuth, ϕ_r	162°	171°	19°	90°
scattering angle, θ	116°	104°	156°	139°

---

[2] Day Of Year

4.1 Measurement Setup

Within 1D radiative transfer, the spatial and temporal variability of clouds is neglected (Deneke, 2002). To overcome this shortcoming, the choice of the spatial and temporal scale has to be sufficiently long to provide a reasonable sampling of the mean irradiance corresponding to the region used in the satellite retrieval. The following averaging scales are used.

Values of the Broadband Atmospheric Transmissivity (BAT) have been obtained from the mean level of irradiance during 10-minute interval, which are archived by pyranometers. Then, an average BAT is calculated from the 4 intervals (i.e. 40 minutes) closest to the time of the satellite overpass, which is used as input to the pyranometer retrieval. These temporally averaged pyranometer measurements have to be considered as statistical samples of the spatially averaged surface irradiance corresponding to the area used for the satellite analysis.

Bi-directional reflectances obtained for an 8 x 8 pixel grid centered on each KNMI pyranometer site are used to relate the satellite retrieval to *in situ* pyranometer observations. This pixel grid corresponds to a region of about 10 x 10 km for a nadir view. The mean of all 8 x 8 individual pixels is calculated by summing over all pixels and finally dividing the sum by the number of pixels.

The size of the chosen spatial and temporal scales is based on the findings of previous investigations of Deneke (2002). However, these findings are based on 6-years of data, assuming the atmosphere only to be cloudy or cloud-free. No selection is done for specific cloud structures. It is therefore expected that large errors will occur due to inaccurate collocation of clouds for specific cloud scenes, e.g. cumuli. The size of the spatial and temporal scales is an important factor for minimizing errors due to inaccurate collocation of clouds. The collocation errors that are also referred to as sampling errors are illustrated in Fig. 4.1.

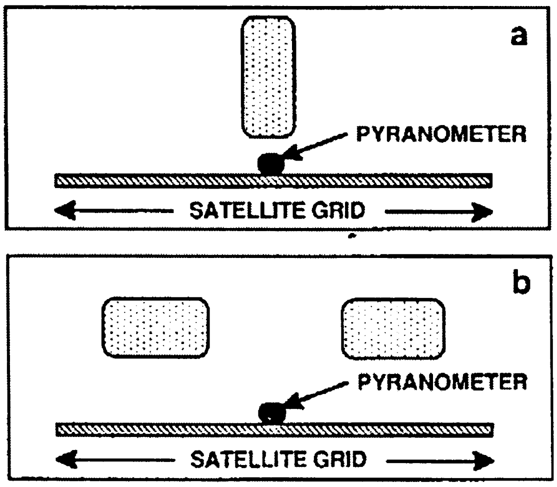

Figure 4.1: Schematic illustration of satellite surface sampling errors caused by broken clouds. (a) A single isolated cloud that impacts the surface measurements while having little effect on the satellite measurement and (b) same as Figure 4.1a, except for clouds over most of the satellite grid but not over the surface (From: Cess *et al.*, 1996).

A significant contributor to measurement errors associated with collocated satellite-surface measurements are sampling errors, which occur because the satellite pixel measurements are instantaneous and represents a grid that is much larger than the field of view of an upward facing pyranometer. As schematically illustrated in Fig. 4.1a, a single isolated cloud could substantially influence the surface measurement while having little effect on the satellite measurement; the reverse would occur if there were clouds over most of the satellite grid but not over the surface instrument (Fig. 4.1b). Cloud systems move, however, so that, in a statistical context, temporally averaging the surface measurements can be equivalent to spatially averaging the satellite measurements. Therefore, care must be taken by comparing measurements obtained by different measuring scales.

Statistic treatment

The relevant statistical measures such as, correlation coefficient, mean, and bias are used for analysis. All are calculated by statistical functions in IDL (Fanning, 1997).

In this study, the correlation coefficient, r, is defined as the ratio of the covariance of the sample populations x and y to the product of their standard deviations

$$r = \frac{\operatorname{cov} ariance\ of\ x\ and\ y}{(s\tan dard\ deviation\ of\ x)(s\tan dard\ deviation\ of\ y)}, \qquad (4.1)$$

or

$$r = \frac{\frac{1}{N-1}\sum_{i=0}^{N-1}\left(x_i - \left[\sum_{k=0}^{N-1}\frac{x_k}{N}\right]\right)\left(y_i - \left[\sum_{k=0}^{N-1}\frac{y_k}{N}\right]\right)}{\sqrt{\frac{1}{N-1}\sum_{i=0}^{N-1}\left(x_i - \left[\sum_{k=0}^{N-1}\frac{x_k}{N}\right]\right)^2}\sqrt{\frac{1}{N-1}\sum_{i=0}^{N-1}\left(y_i - \left[\sum_{k=0}^{N-1}\frac{y_k}{N}\right]\right)^2}}, \qquad (4.2)$$

where N represents a two n-element sample population of x and y. The correlation coefficient is a direct measure of how well two sample populations vary jointly. A value of $r = +1$ or $r = -1$ indicates a perfect fit to a positive or negative linear model, respectively. A value of r close to +1 or -1 indicates a high degree of correlation and a good fit to a linear model. A value of r close to 0 indicates a poor fit to a linear model. However, this does not mean that there is no correlation between the two sample populations. It is possible that the relationship between x and y is accurately described by a non-linear model.

The mean is referred to as the statistical mean of the 40-minute pyranometer measurement interval. The latter is used as ground truth. Bias represents the differences between the satellite and pyranometer mean. A positive or negative bias indicates that the mean of the satellite measurements is higher or lower than the pyranometer mean, respectively. A root-mean-square-error (RMSE) and a linear regression function are also given. The latter have the form

$$y_i = bx_i + a. \qquad (4.3)$$

The y variable can be expressed in terms of a constant (a) and a slope (b) times the x variable. The constant is also referred to as the *intercept*, and the slope as the *regression coefficient* or *b coefficient*. In IDL, the program 'Sixlin' is used to derive a regression function. This program contains of six different methods to derive a regression function. The method used in this thesis is based on the Ordinary Least Squares Bisector method, which treats scatter in both x and y variables symmetrically and performs best for noisy datasets. This method is recommended in case of determining the functional relationship between x and y (Deneke, 2002). As for the RMSE, this is calculated as the standard deviation of individual points from the regression line according to

$$RMSE = \sqrt{\frac{1}{N}\sum_{i=1}^{N}\{y_i - y(x_i)\}^2}, \qquad (4.4)$$

N = sample population of y
y_i = measurement
$y(x_i) = x_i$ calculated with the regression function

Eq. 4.4 derives the RMSE from the values of residuals over all data points. For each component (x_i or y_i), the residuals are defined as differences between the coordinates at this point calculated with the regression function. The RMSE is sensitive for outliers, since every individual point has the same weighting factor. The way outliers are distributed in a scatter plot is an important indicator for the occurrence of random or systematic error.

Random error is caused by any factors that randomly affect measurement of the variable across the sample. This type of error occurs when, for instance, natural variability of atmospheric constituents (gases, aerosol, clouds) is not taken into account by a RTM. The important property of random error is that it adds variability to the data but does not affect the mean. Because of this, *random* error is sometimes considered *noise*.

Systematic error is caused by any factors that systematically affect measurement of the variable across the sample, e.g. thermal offset of the pyranometer's measuring device. Unlike random error, systematic error tends to be consistently either positive or negative. Because of this, *systematic* error is sometimes considered *bias* in measurements.

4.2 Case I: Clear Sky

a) Meteorological conditions

Fig. 4.2 (a and b) shows Europe as observed from the NOAA-14 polar satellite by AVHRR channel 1 (0.63 μm) and channel 4 (10.8 μm) on 28 July 1999 at 14:32 UTC. The white pixels on both images have different meanings. As for Fig. 4.2a, white pixels refer to high reflectivities, where white pixels on the IR image (Fig. 4.2b) refer to low (cloud) temperatures. The absences of white pixels in The Netherlands region indicate clear-sky. This latter is not valid for the Alps region and the Pyrenees. As for this region low cloud top temperatures indicates presumably vertically well developed clouds. A consistent cloud field is covering a significant part of the North Sea and the north part of the Atlantic Ocean with a sharp boundary between the cloud field and the west coast of Norway. This is also seen on the IR image. A small difference in grey tone is indicating small temperature differences between the cloud field and the North Sea. Hence, low cloud tops can be assumed. Furthermore, a nice sun glint[3] is seen on the visible image at the Mediterranean Sea between Spain and Algeria.

A high-pressure area dominated the meteorological conditions in the Netherlands, causing a northeasterly wind (60 degrees) with a speed of approximately 12 knots. At 14:00 UTC, synops observations reported zero oktas of cloud cover at the meteorological stations of KNMI. The air pressure is around 1020 hPa with maximum air temperatures of almost 26°C.

b) Comparison of Retrieval Results

In this paragraph, the satellite retrieved downwelling solar surface irradiances (DSSI) are compared with ground-based pyranometer measurements. In particular, the DSSI and atmospheric transmissivities are compared.

Fig. 4.5 shows the clear sky DSSI obtained from the satellite retrieval and pyranometer measurements. In this figure, mean, correlation coefficient, bias, a linear regression function, and a root mean square error (RMSE) are listed.

The slope and offset (or bias) of the regression function are showing values of 0.667 and 246.3 W m^{-2}, respectively. This is a deviation from the desired value of unity and zero. The measurements show some variability with respect to the regression line. The latter indicates random error. To explain the deviant behaviour of the measurements shown in Fig. 4.5, the procedure for obtaining DSSI is analysed in more detail.

According to Equation 2.7, the solar constant and its angle relative to the normal of the Earth's surface are assumed constant for a single satellite overpass. The only free parameter in this equation is the broadband atmospheric transmissivity (BAT). The BAT will be analysed later on in this section. First, the cosine of the solar zenith angle, μ_0, is analysed. This parameter is calculated separately for both the AVHRR and the pyranometer retrieval and is shown in Fig. 4.6. The reason for calculating the μ_0 separately is historically determined (Feijt, pers. comm.).

In Fig. 4.6, it can be seen that the μ_0 compared to the one-to-one line is showing a bias in viewing geometry for this clear-sky case. The bias has a value of 2.1%. In theory, there should be no difference between the two calculated solar zenith angles. Therefore, a correction factor of 0.979 is used to eliminate this bias. The correction factor represents the difference between the bias and the one-to-one line. The impact of this correction is shown in Fig. 4.7. The bias is decreased to 2.9 W m^{-2}. Both slope and offset of the regression line have also decreased. The correlation coefficient and RMSE remains practically the same. This is expected, since the μ_0-correction is applied to all the data points in a similar way. Further, the magnitude of the offset presented in Fig. 4.5 and 4.7 can be explain by the small range of the plotted values. As the DSSI are only plotted between 650 and 750 W m^{-2}, it is expected that small changes will induce large changes in offset.

---

[3] Sun glint is a bright spot on the visible image caused by the sunlight reflecting from a smooth surface

Figure 4.2a: AVHRR channel 1 image of Europe at 14:32 UTC on 28 July 1999 (DUNDEE).

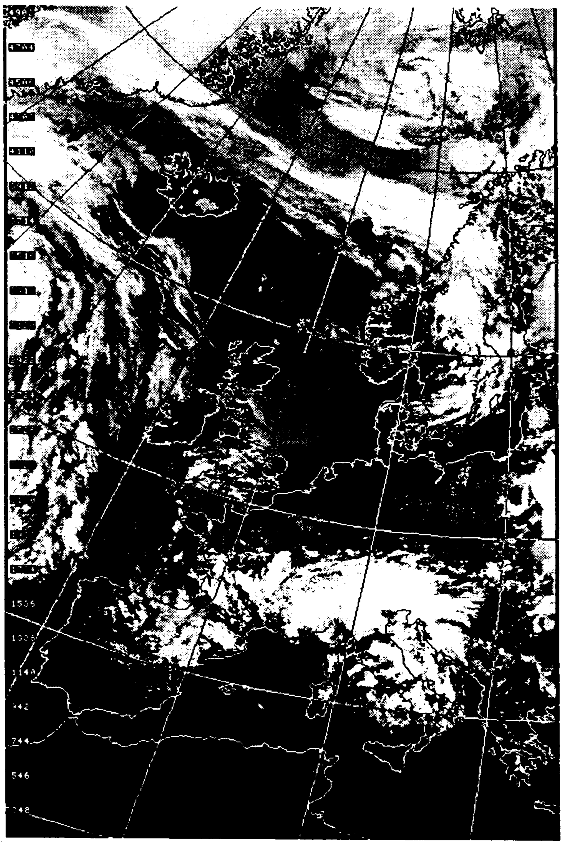

Figure 4.2b: AVHRR channel 4 image of Europe at 14:32 UTC on 28 July 1999 (DUNDEE).

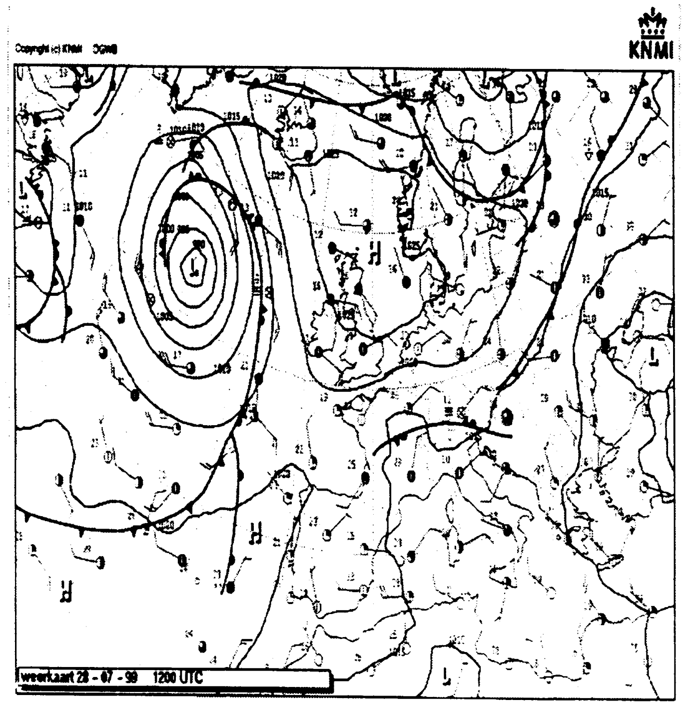

Figure 4.3: Weather map of Europe valid for 12:00UTC on 28 July 1999.

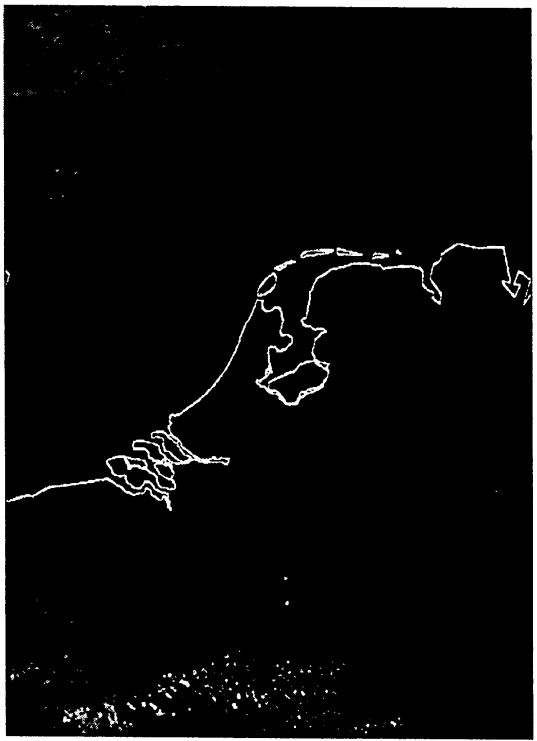

Figure 4.4: AVHRR channel 1 image of The Netherlands at 14:32 UTC on 28 July 1999 (KLAROS). Black areas correspond to clear surface.

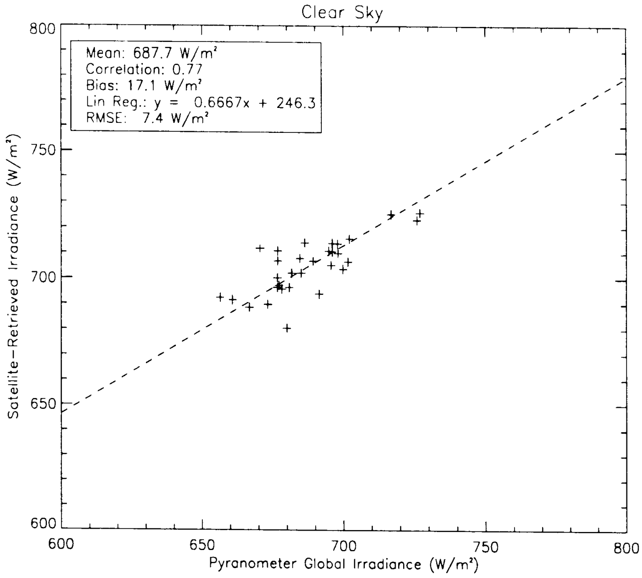

Figure 4.5: Scatter plot of satellite-retrieved and pyranometer measured downwelling solar surface irradiance.

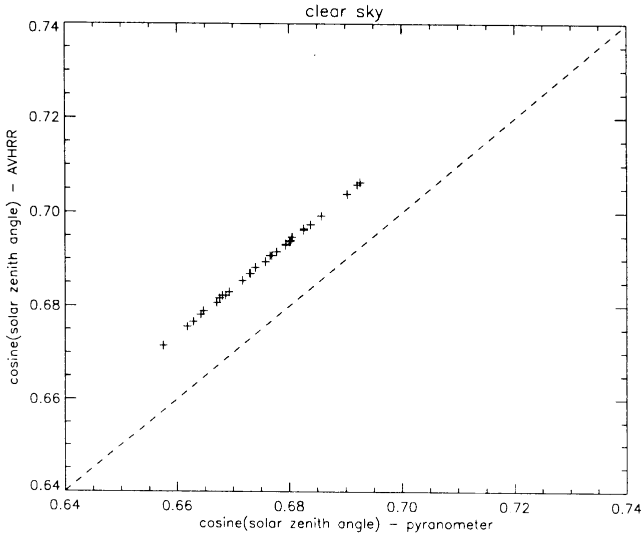

Figure 4.6: Difference in calculations of the solar zenith angle, calculated by pyranometer (for 32 locations) and AVHRR for a single satellite overpass at 14:32 UTC.

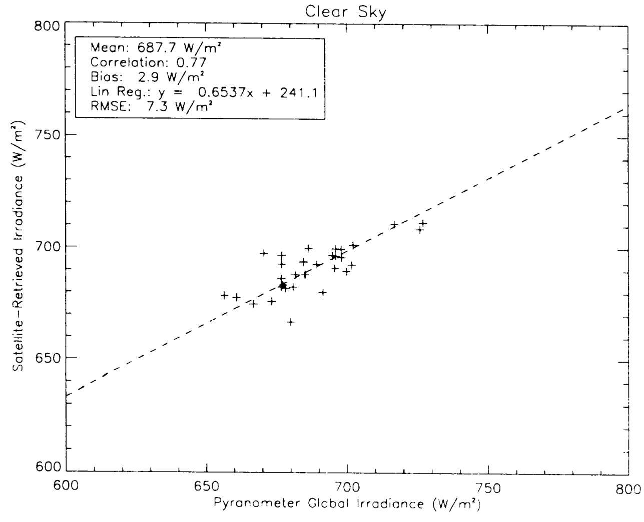

Figure 4.7: As in Fig. 4.5 except that satellite-retrieved downwelling solar irradiances are multiplied by a μ_0-correction.

Fig. 4.8 shows the relationship between retrieved satellite transmissivities and those calculated from solar irradiance measurements by pyranometers. As for the BAT, it shows less dependence on the μ_0 than the DSSI, since the variability of the DSSI caused by changes of the incident TOA irradiance is removed. Also, it is seen that the difference in satellite derived transmissivities is much smaller than those derived from pyranometer measurements.

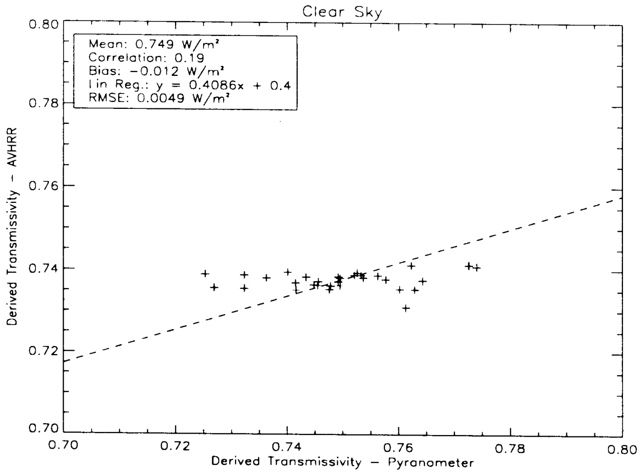

Figure 4.8: Broadband Atmospheric Transmissivity values obtained by both pyranometer and AVHRR -μ_0 corrected - measurements.

For this clear sky case, the BAT values are directly retrieved from the pyranometer lookup table. The results are in Fig. 4.9a. This procedure contains the following steps. If the satellite-measured reflectivity of a pixel falls below 'clear-sky' threshold, the pixel is assumed cloud-free. However, the RTM accounts only for clouds. For cloud-free pixels, the cloud optical depth is then set to zero in both LUTs. Hence, the transmissivity of these pixels is directly obtained from the pyranometer LUT, assuming a standard atmosphere and a measured integrated water vapour (IWV) path. The latter is taken constant for a single satellite overpass. This means that variations in satellite retrieved BAT can only be explained due to variation in viewing geometry. This explains the small difference in satellite retrieved BAT shown in Fig. 4.8.

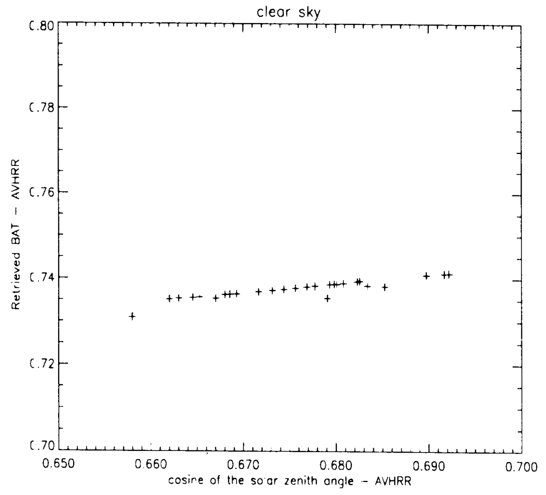

Figure 4.9a: AVHRR retrieved BAT as a function of the corrected solar zenith angle μ_0 at 13:59 UTC.

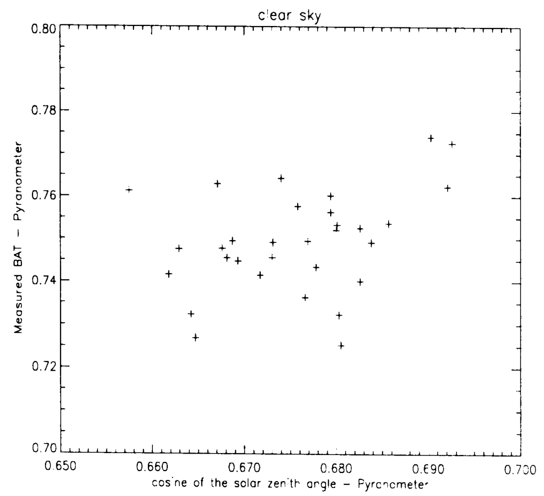

Figure 4.9b: As in (a) except this is for 10-min average measured BAT obtained by pyranometers.

In Fig. 4.9a, a small increase in BAT is seen with increasing μ_0. This is expected since the satellite LUT is treating all atmospheric parameters as constant values, except for the solar zenith angle, μ_0. Therefore, the behaviour of the BAT can only be explained by the dependency of the Sun elevation to the optical path of sunlight through the Earth's atmosphere. The optical path increases with decreasing Sun elevation. This means that the probability of a photon to be absorbed or scattered by the Earth's atmosphere increases as well. Therefore, the atmosphere is said to become less transparent than for a shorter optical path.

The variability of BAT, shown in Fig. 4.9b, is the actual variability in atmospheric transmittance measured by pyranometers. These measurements are showing more variability than those retrieved from the LUT. This results in a RMSE of 0.017 that is 2.3% of the mean BAT. Differences between calculated BATs presented in Fig. 4.9a and the observations presented in Fig. 4.9b are caused by spatial and temporal variability of atmospheric water vapour, aerosol concentration, and surface albedo at the 32 KNMI sites throughout The Netherlands. Deneke (2002) found for clear skies that changes in the integrated water vapour (IWV) column and aerosol concentration have by far the largest impact on the atmospheric transmissivity, leading to variations of several percent. Changes in temperature, pressure and ozone column only cause minor variations with maximum values of up to a quarter of percent.

c) Conclusions

The correspondence between the satellite retrieved and ground-based measured DSSI was generally good, yielding a small bias of 2.9 W m^{-2} (after correction for the offset in calculations of the solar zenith angle). The latter is only 0.4% of the mean irradiance. The corrected bias of the retrieval results remains within the boundaries of the estimated pyranometer calibration accuracy of 5%.

We have further noted a higher variability of atmospheric transmissivity in the pyranometer measurements than in the output of the satellite retrieval. We found a RMSE of 0.017 that is 2.3% of the mean BAT. This is possibly related to the representation of spatial variability of atmospheric constituents that is not accounted for by the RTM. This is a limitation, since spatial variation in IWV and aerosol concentration can lead to significant deviation in retrieving DSSI. However, this limitation also marks the boundary conditions of the satellite retrieval. The assumption of an isotropic and constant surface albedo is also a limitation of the retrieval schemes in its current form. Due to the variability introduced by different surface types, seasonal change in the state of vegetation, and the dependence on solar zenith angle, errors of several percent are expected to occur either in form of random noise or as bias. It is possible that there was some cloud contamination, despite the fact that the AVHRR pixels where flagged cloud free, as they were assumed to be. In addition, the existence of thin cirrus and contrails would give a possible error. Another possible error source are calibration errors of the pyranometers. The existence of the thermal offset and the possibility of the calibration can lead to a significantly large measurement uncertainty (Deneke, 2002). The impact of possible cloud contamination and instrumental calibration errors on the results is not known.

4.3 Case II: Overcast

In contrast with the previous section, this section presents two cases that are selected from ten overcast conditions. First, Fig. 4.10 shows the comparison of AVHRR retrieved and pyranometer measured DSSI based on ten overcast situations.

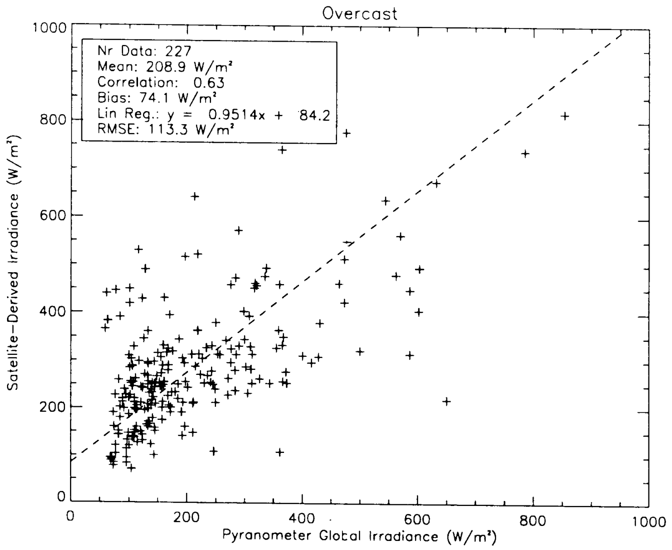

Figure 4.10: AVHRR retrieved and pyranometer measured DSSI values obtained for ten overcast situations.

Some synops observations of the selected overcast situations recorded precipitation values, which can be a possible explanation of the overall RMSE of 113.3 W m^{-2} (i.e. 54% of the mean irradiance) shown in Fig. 4.10. To analyse this, two overcast situations are selected based on their precipitation records. The first case (2 May 2000) is selected on a record that has no precipitation, while for the second case (22 July 1999) precipitation has been recorded.

1. May 2nd 2000 (No-precipitation)

1a) Meteorological conditions

Fig. 4.11 (a and b) shows Europe as seen by channel 1 and 4 of the AVHRR instrument. A cloud field is covering the northwest part of France and also Belgium and The Netherlands. Due to the small difference in grey tone between the land surface and the clouds seen in Fig. 4.11b, low clouds are expected for this region. Fig. 4.13 is obtained by KLAROS. This image shows that the colour of the cloud deck does not differ much spatially. Only the brighter white pixels in the east part of this image indicate heterogeneous clouds. The latter is possibly a remainder of the frontal system passing The Netherlands around 12:00 UTC. This frontal system is plotted on the weather map in Fig. 4.12. The time difference between Fig. 4.12 and the AVHRR images is approximately 3 hours. During this period, the frontal system has likely moved to the east of The Netherlands.

According to synops observations, the cloud base height varies between 1000 and 1300m. Furthermore, eight oktas of cloud cover are reported for the low and middle cloud layer. The average wind direction and wind speed are 20° and 11 knots, respectively. The surface pressure during the passage of the front was relatively high at 1020 hPa.

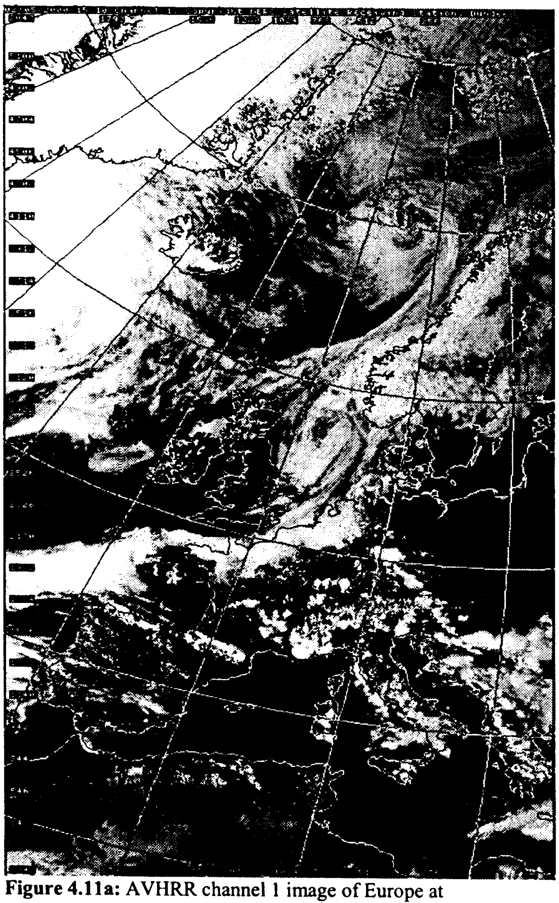

Figure 4.11a: AVHRR channel 1 image of Europe at 15:09 UTC on 2 May 2000 (DUNDEE).

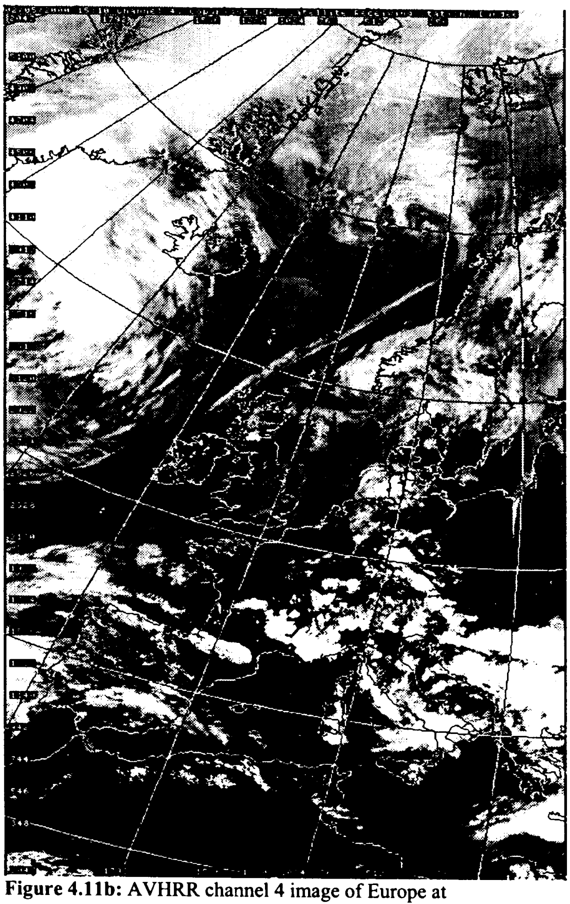

Figure 4.11b: AVHRR channel 4 image of Europe at 15:09 UTC on 2 May 2000 (DUNDEE).

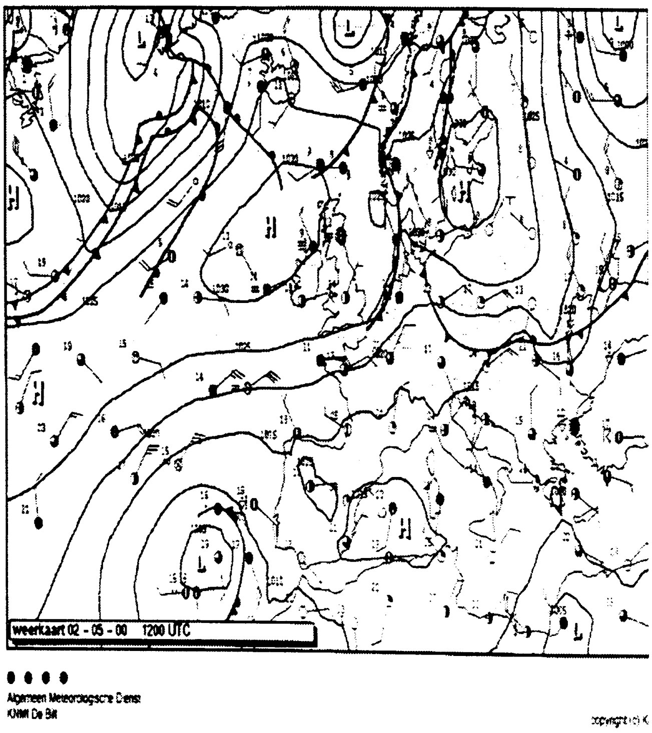

Figure 4.12: Weather map of Europe valid for 12:00 UTC on 2 May 2000

Figure 4.13: AVHRR channel 1 image of The Netherlands at 15:09 UTC on 2 May 2000 (KLAROS).

1b) Comparison of Retrieval Results

An important aspect of the retrievals is the correct representation of cloud optical properties in the RTM. As ice crystals and water droplets have rather different phase functions, the correct choice is expected to lead to a significant improvement in retrieval accuracy. Classification of the cloud phase in the RTM consisting of either ice crystals or water droplets is chosen *a priori*. Here, the phase of the cloud layer is assumed liquid. This assumption is based on KLAROS analysis of the AVHRR Channel 4.

Fig. 4.14 (a and b) shows channel 4 IR temperatures obtained for The Netherlands at the time of the noon-overpass of NOAA-14. The IR temperatures are concentrated between the 275 and 280 K interval. According to synops observations, the surface temperature is approximately 285 K. This implies that the IR temperatures shown in Fig. 4.14a correspond to temperatures of the cloud layer. However, Fig. 4.14b shows a small fraction of IR temperatures that are between 260 and 273 K. From this point, it is not clear whether the cloud particles within this temperature range consist of ice crystals or water droplets. However, the fraction of these cloud particles is relatively low. The cloud layer is therefore assumed liquid.

Another aspect of Fig. 4.14b is the distinct peak at approximately 278 K and the low variability of IR temperatures. This implies that the cloud layer has also low variability in the vertical. Therefore, it is expected that the cloud layer is in agreement with the assumption of a homogenous plane parallel cloud (PPH) in the RTM. The latter is an important requisite for radiative transfer calculations, since cloud inhomogeneity is not accounted for by the RTM.

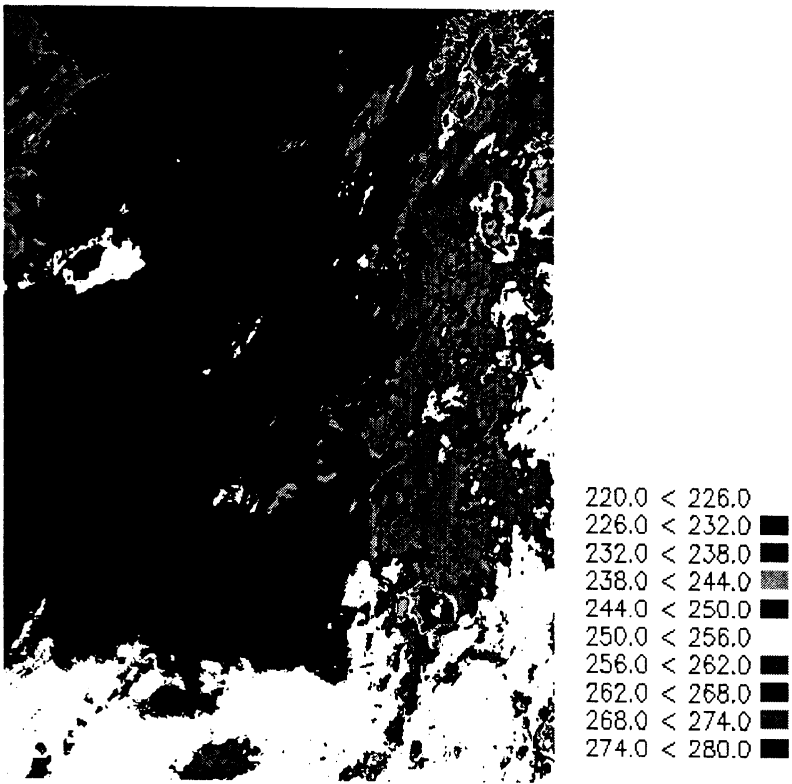

Figure 4.14a: AVHRR 10.8 μm IR temperature (K). White areas are clear surface.

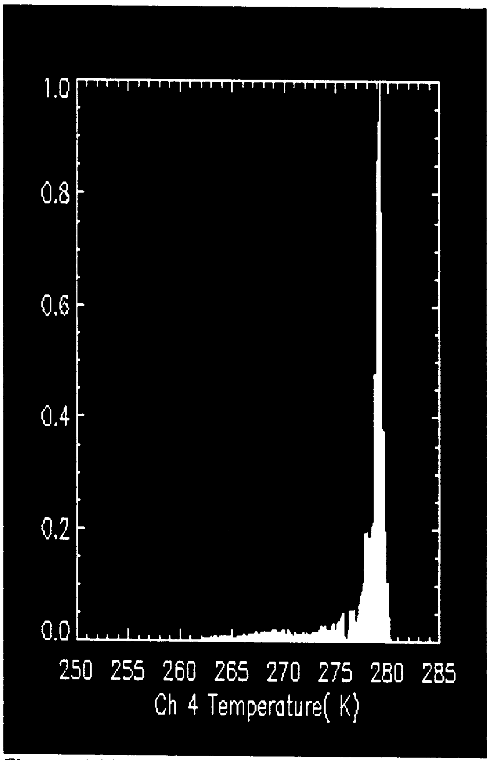

Figure 4.14b: Temperature histogram of AVHRR Channel 4 obtained for The Netherlands on 2 May 2000.

Results of the satellite retrieval of the DSSI are shown in Fig. 4.15 in comparison to values obtained from individual pyranometer measurements

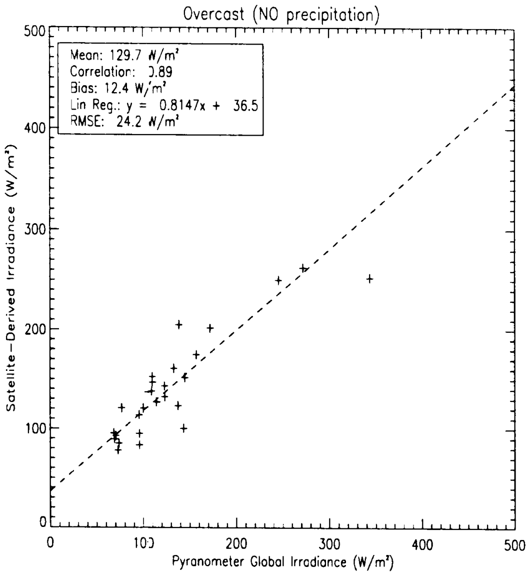

Figure 4.15: Comparison of downwelling solar surface irradiance for all pyranometer measurements available for a single satellite overpass on 2 May 2000.

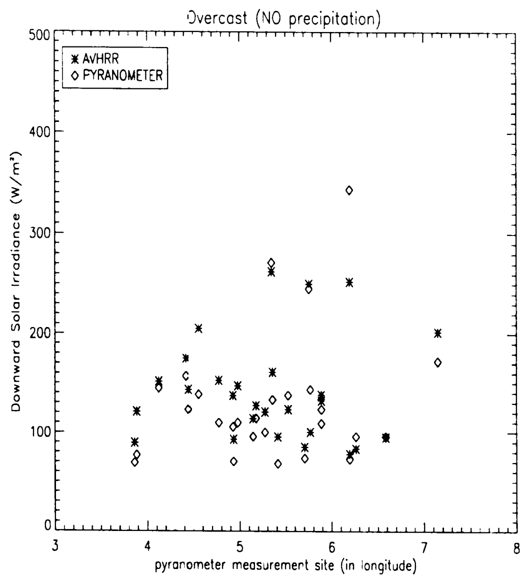

Figure 4.16: Difference between measured and retrieved DSSI obtained for all KNMI pyranometer sites in The Netherlands for a single satellite overpass at 15:09 UTC on 2 May 2000.

In Fig. 4.15, values are found for the correlation coefficient and the RMSE, having magnitudes of 0.89 and 24.2 W m^{-2}, respectively. Further, a bias of 12.4 W m^{-2} is found, which is 9.6 % of the mean. The deviations between measured and calculated DSSI plotted for every single pyranometer site, are shown in Fig. 4.16. This figure shows an overall tendency of slightly higher DSSI values obtained by the AVHRR.

It is assumed that the overall accuracy of the calibration of both instruments is not exceeding 5% (see Ch 3). Hence, it is expected that the remnant of the bias in Fig. 4.15 is due to atmospheric uncertainties in the RTM. To investigate these uncertainties, the cloud optical depth is used. This parameter is chosen, because significant deviations of the measured transmissivity/ reflectivity may have large impact on the retrieved cloud optical depth. This is due to the non-linear relationship of the transmissivity/ reflectivity to the cloud optical depth. Fig. 4.17 shows cloud optical depths retrieved from both pyranometer and satellite measurements.

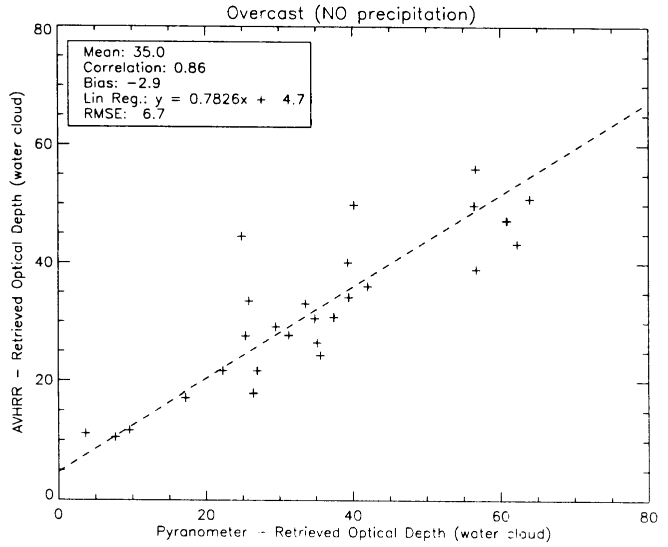

Figure 4.17: Comparison of cloud optical depths retrieved from broadband solar irradiances at the surface and 0.63 μm TAO reflectances.

As stated in Ch. 3, results exceeding a cloud optical depth above 80 and 50 for water and ice clouds, respectively, in any one of the two retrievals are rejected. The retrieval functions become too sensitive to instrumental and modelling errors at larger values of the optical depth for reliable results (Deneke, 2002). Fig. 4.17 shows a bias of –2.9. This means that the retrieved cloud optical depths of overcast clouds tend to be slightly less for the satellite than for the pyranometer. This means that the satellite retrieval assumes thinner clouds. The underestimation of the cloud optical depth will lead to an overestimation of the satellite retrieved DSSI. This latter is in agreement with the results shown in Fig. 4.15 and 4.16.

2. July 22nd 1999 (Precipitation)

2a) Meteorological conditions

Fig. 4.18 (a and b) show Europe as seen by the AVHRR channel 1 and 4 image respectively on 22 July at 13:59 UTC. The brightness of the pixels in Fig. 4.18b indicates that the cloud field covering The Netherlands contains low IR temperatures. This cloud field is marked as an occlusion front on the weather map shown in Fig. 4.19. Behind the occlusion front, there is another (cold) front. Since this weather map is valid for 12:00 UTC, it is expected that a front is passing by The Netherlands at the time of the noon-overpass of NOAA-14. Furthermore, a high-pressure area is seen on this map at the southwest of Ireland, causing a (north) westerly wind for The Netherlands. However, due to passing frontal systems, the wind direction and wind speed are variable.

Fig. 4.20 and 4.21 are made with KLAROS, showing The Netherlands as seen by AVHRR channel 1 and 4 at 13:59 UTC. Fig. 4.20 shows a distinct overcast situation with relatively bright white pixels for the east /southeast and the north of The Netherlands. In Fig. 4.21, these pixels correspond to IR temperatures below 260 K. The lowest IR temperatures are seen in the mid-east of the Netherlands, having values of approximately 230 K, indicating vertical cloud development.

According to synoptic observations, the surface temperatures at 2m above surface are around 15 ^{0}C at the time of the NOAA overpass. The height of the cloud base varies between 600 and 1600m. Synops observations are reporting eight oktas of cloud cover for the low- and midlevel cloud layer. Also, a considerable amount of precipitation is recorded during this day. The highest 'total sum' value is recorded at station 'Marknesse' (12.9 mm in 8.8 hours). Station 'Eelde' recorded 11.2 mm precipitation in less than 10.8 hours and station 'Twenthe' had a 'total sum' value 10.8 mm in less than 7.5 hours.

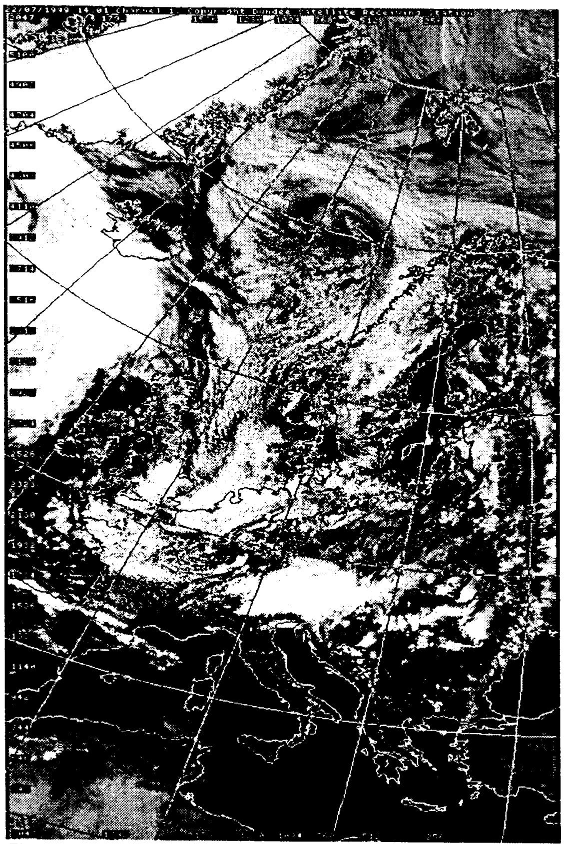

Figure 4.18a: AVHRR channel 1 image of Europe at 13:59 UTC on 22 July 1999 (DUNDEE).

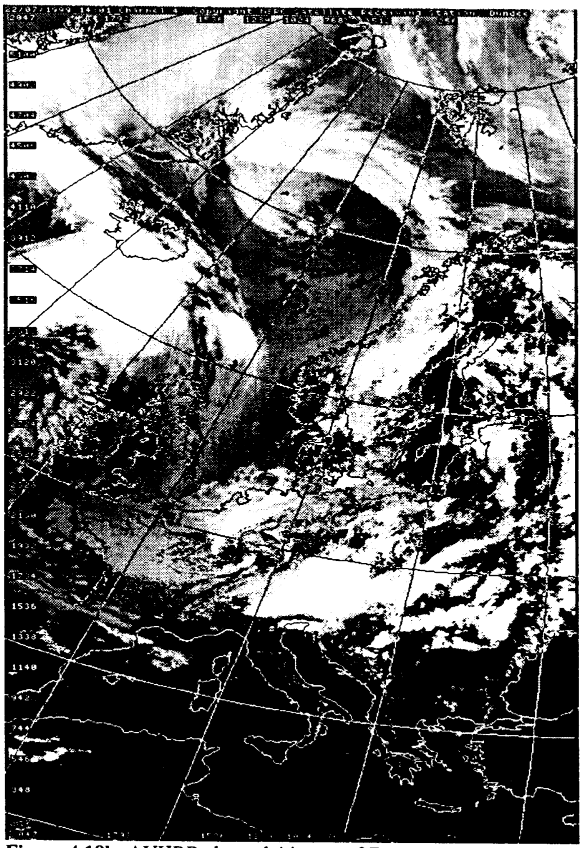

Figure 4.18b: AVHRR channel 4 image of Europe at 13:59 UTC on 22 July 1999 (DUNDEE).

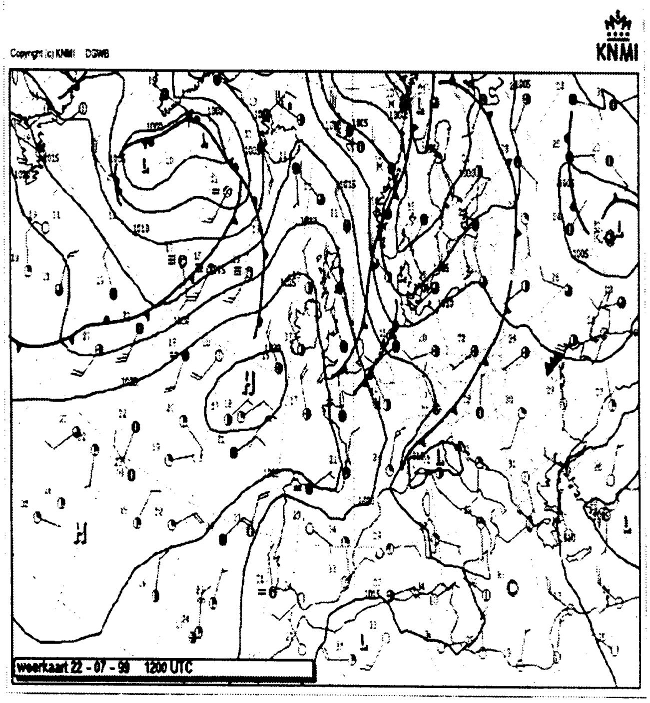

Figure 4.19: Weather map of Europe valid for 12:00 UTC on 22 July 1999.

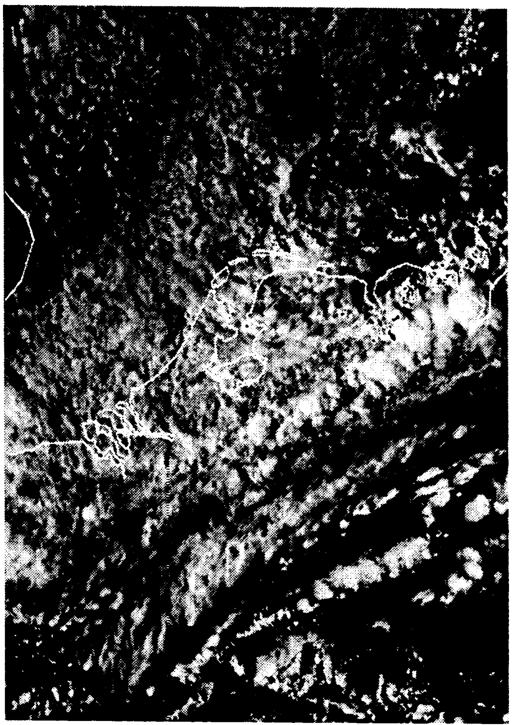

Figure 4.20: AVHRR channel 1 image of the Netherlands at 13:59 UTC on 22 July 1999 (KLAROS).

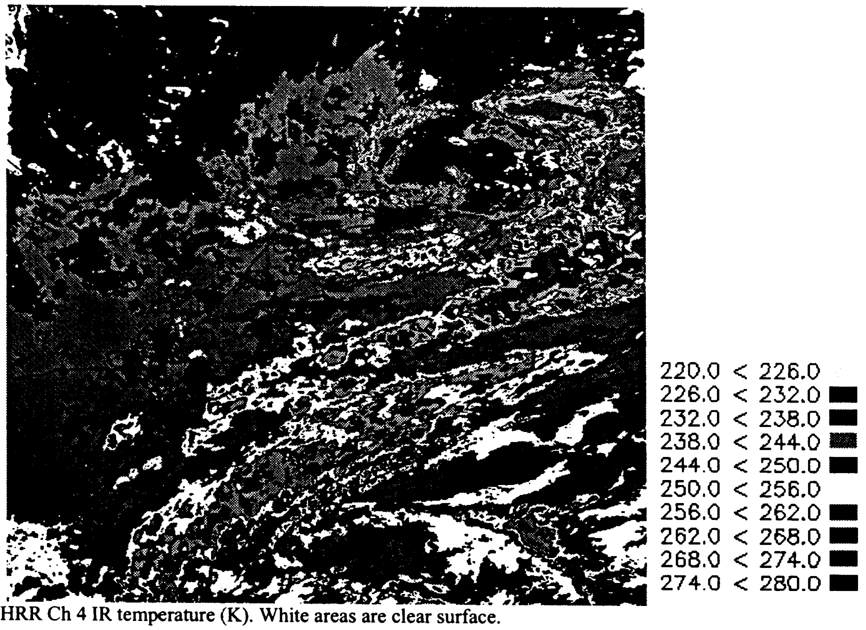

Figure 4.21: AVHRR Ch 4 IR temperature (K). White areas are clear surface.

2b) Comparison of Retrieval Results

The results of the satellite retrieval of the DSSI in comparison to values obtained from individual pyranometer measurements are shown in Fig 4.22. Correspondence of the measurements with the retrieved values shows a bias of 115.3 W m^{-2}. This is 88% of the mean. Several mechanisms are assumed to contribute to this high bias. These mechanisms are:

- 3D cloud structures
- Assumption of the cloud particle size distribution and cloud phase in the RTM
- Contamination of the pyranometer domes due to rainfall

Since there is hardly any correlation between the satellite and ground based datasets for this precipitation case, no regression has been made. The dashed line in the following figures represents the one-to-one line. As for Fig. 4.23, the comparison between measured and retrieved DSSI are plotted for every single pyranometer site of KNMI. Large differences between the measured and calculated DSSI can be seen in this figure. To get a better understanding of the discrepancies, the mechanisms mentioned above are studied in more detail.

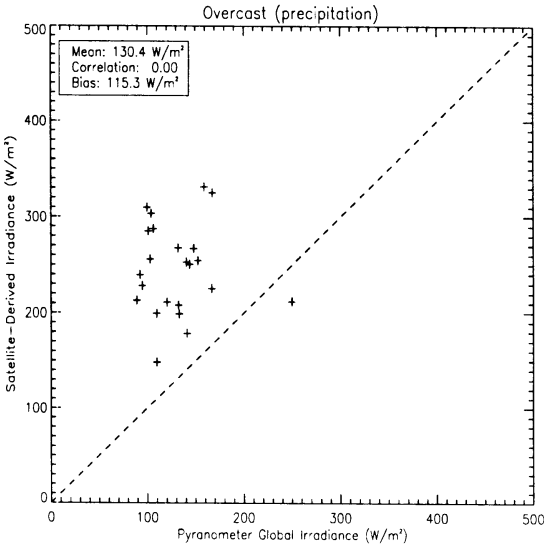

Figure 4.22: Comparison of retrieved downwelling solar surface irradiance (assuming water cloud) for all pyranometer measurements available for a single satellite overpass on 22 July 1999.

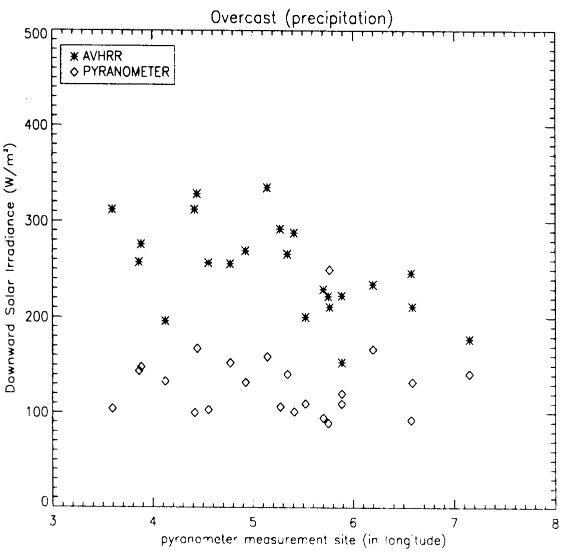

Figure 4.23: As in Fig. 4.22, except that the DSSI is a function for all KNMI pyranometer sites in The Netherlands.

The satellite retrieval using plane-parallel radiative transfer for its calculations on irradiances in cloudy atmosphere, which is based on mean atmospheric conditions defined in the radiative transfer model. This means that cloud inhomogeneity is not considered in the model settings. Errors are therefore expected in the form of bias. It is important to note that large errors in cloud optical depths may result from small errors in reflectivity/ transmissivity measurements, as the retrieval error grows approximately proportionally with the magnitude of the cloud optical depth. This is due to the non-linearity of both retrieval functions. As an example, when a vertically extended cloud is illuminated at one side, the other side of the cloud will be underexposed. In literature, it is said that the satellite is 'seeing' cloud holes (i.e. optically thinner cloud). If changes in measured reflectivity are in the order of ± 2%, this does not mean that changes in retrieved cloud optical depth are of similar magnitude (see Fig.3.5).

Fig. 4.20 and 4.21 indicate convective clouds (large difference in IR temperatures) in the east of The Netherlands. These clouds probably have three-dimensional structures. As the solar zenith angle is not zero for this case, the spatial variability of the clouds is causing specific areas to be over- and underexposed at the top of the cloud layer. Underexposed areas (shadows) can actually be seen as relatively dark spots in the visible image of Fig. 4.20. The satellite interprets shaded areas as thinner clouds. The satellite retrieval will therefore underestimate cloud optical depths for these shaded areas. This leads to an overestimation of the DSSI. The optically brighter spots in the satellite image will induce the opposite effect.

Despite the magnitude of shading on the DSSI retrieval, it is expected that the relatively darker and brighter spots are not the most important mechanism leading to the large discrepancies shown in Fig. 4.22 and 4.23.

Larger errors are expected due to the assumption of non-precipitating homogenous clouds in the RTM that is not met. For this overcast case, all data are collected during rainfall events (according to synops). Fig. 4.24 is showing cloud optical depths retrieved from both pyranometer and satellite measurements.

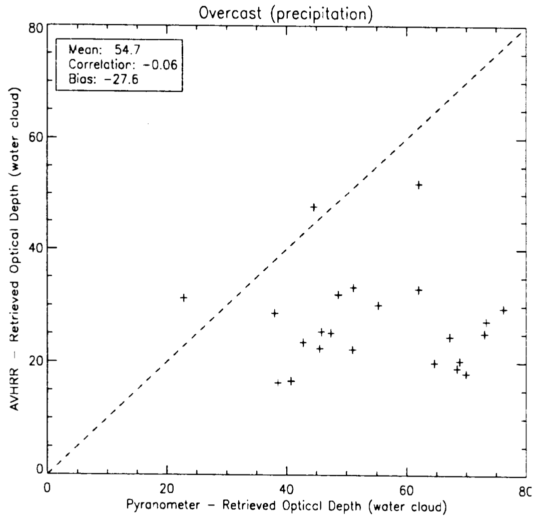

Figure 4.24: Retrieved optical depths from AVHRR bi-directional reflectance and pyranometer BAT (both retrievals assuming a PPH water cloud).

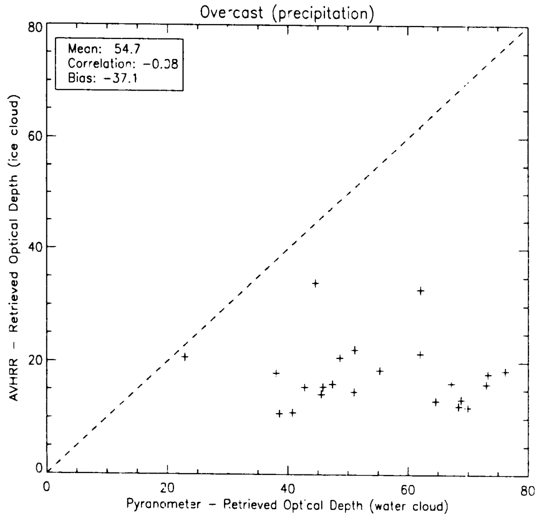

Figure 4.25: As in Fig. 4.24, except that the satellite retrieval assumes a PPH ice cloud.

Since the cloud optical depth is closely related to the cloud water present within a vertical column, it is seen in Fig. 4.24 that the tendency is $\tau_{pyrano} > \tau_{AVHRR}$ and often $\tau_{pyrano} >> \tau_{AVHRR}$. This is mostly attributed to absorption in the NIR of the solar spectrum by the larger cloud particles, e.g. rain droplets and ice crystals. As rain droplets absorb more in the NIR of the solar spectrum than small cloud droplets, retrieved cloud optical depths will be overestimated and hence the DSSI underestimated. This is because absorption by rain droplets is not taken into account in the radiative transfer calculations. The absorption is causing the atmosphere to be optically darker. This results in reduction of measured and retrieved DSSI. However, the reduction in atmospheric transmissivity below the cloud layer due to rainfall is not proportional to the absorption characteristics of the atmosphere described in the RTM. This induces a bias in retrieving cloud optical depths, as shown in Fig. 4.24.

During rainfall, ice crystals are formed at the top of a cloud layer. Since the cloud layer is vertically non-homogeneous in this overcast case, the corresponding cloud top temperatures are also non-homogenous. This is illustrated in Fig. 4.21. This figure shows the IR temperature of the cloud layer. Since the cloud layer is assumed thick ($\tau > 5$), the IR values are corresponding to cloud top temperatures. It can be seen that a significant part of the cloud layer have IR values between 260 and 274 K. Therefore, a water cloud is assumed in both retrieval schemes. However, small fractions of the cloud layer show IR values of less than 250 K. Cloud tops in this region probably consist of ice crystals. According to the assumptions made in the RTM, a cloud consists either of ice particles, or cloud droplets. This assumption is physically not a correct representation of the actual atmospheric conditions. Fig. 4.25 shows the results if an ice cloud is assumed in the satellite retrieval and a water cloud in the pyranometer retrieval. The bias in retrieved cloud optical depth increases to –37.1, indicating that this assumption is not in better physical agreement with the actual atmospheric conditions. A significant part of the bias, shown in Fig. 4.24. and 4.25, is presumably due to contamination of the pyranometer domes (i.e. rain droplets disturb radiation fluxes entering the domes). However, no further information is available about the expected sign and magnitude of the bias due to the contamination of the pyranometer domes on the measurements. Further research has to be done to quantify the error due to this form of contamination.

c) Conclusions

The results presented in this section show that discrimination of non-precipitating and precipitation case is desirable for comparison of retrieved values with *in situ* pyranometer measurements. As for the non-precipitation case, the DSSI retrieval is capable of capturing the influence of the homogenous cloud well, resulting in a correlation coefficient of 0.89 and a bias of 12.4 W m^{-2}. The latter is 9.6% of the mean. However, for the precipitation case, the comparison between satellite retrieved and pyranometer measured DSSI is not showing any correlation. A number of possible explanations for the observed discrepancies are classification of the cloud phase, the absorption characteristics in the RTM and contamination of pyranometer domes during rainfall. Realistic values of IR temperatures show the existence of both water droplets and ice crystals. Since the RTM does not account for mixed-phase clouds, errors are expected in form of noise and bias due to this limitation.

Furthermore, a significant loss in accuracy of RTM in form of systematic errors is expected if rain events occur. Rain droplets absorb more in the NIR of the solar spectrum than small cloud particles. There is no assumption in the RTM in its current form, which accounts for the absorption characteristics of rain droplets. Quantifying the effect of the contamination of pyranometer domes due to rain droplets is also desirable, since the impact on measurements is not thoroughly understood.

For future research, it is recommended to use additional instruments for discriminating precipitation events from non-precipitation (e.g. Doppler radar). It is expected that with this discrimination, the retrievals will increase in accuracy significantly.

4.4 Case III: Broken Clouds

Analysis of retrieval schemes, based on 1D radiative transfer is difficult in case of broken clouds. Due to the broken structure of a cloud field, errors in the form of noise and bias are expected in the retrieval results. This is because the RTM is expected to lose accuracy when there is high horizontal and vertical cloud relief. This is due to the assumption of horizontal homogeneity made in the RTM. The collocation error, that is particularly more sensitive when horizontally inhomogeneous clouds or broken clouds are present, is important in broken cloud conditions. Spatial and temporal averaging scales have to be chosen in such way that these scales be in agreement with the observed cloud structure.

a) Meteorological conditions

24 June 1999 was selected from synops observations as a 'broken clouds' case. A northwesterly flow was advecting air over the relative cool North Sea, picking up enough moisture to generate and maintain cumuli in The Netherlands.

Figure 4.26 (a and b) is showing Europe, as observed by the NOAA-14 satellite. The visible image (0.63 μm) of AVHRR shows large cumuli fields covering The Netherlands, Belgium, central Scandinavia, and parts of Germany. These cumuli fields are characterized by clusters of bright white pixels and by their sharp boundaries near the coast.

The weather map (Fig. 4.27) shows a high-pressure area situated above the North Sea, causing sunny weather conditions in this area. Also seen in this figure is the large distance of lines of constant pressure (isobars). This indicates mild and variable winds across The Netherlands.

Synoptic observations in The Netherlands recorded air temperatures at 2m above ground level around 18 ^{0}C. These observations are recorded at 14:00 UTC. The cloud base height varies between 1600-2000m. According to the height of the cloud base, all clouds in this study are therefore assumed liquid. Synops observations reported cloud codes 2 and 8 for the low cloud layer. These codes correspond to the following cloud description:

- Cloud Code 2: Cumulus of moderate or strong vertical extent, generally with protuberances in the form of domes or towers, either accompanied or not by other Cumulus or by Stratocumulus, all having their bases at the same level

- Cloud Code 8: Cumulus and Stratocumulus other than that formed from the spreading out of Cumulus; the base of the Cumulus is at a different level from that of the Stratocumulus
  (Source: http://www.weather.org.uk/resource/cld_code.htm)

Furthermore, at the coastal areas, the wind speed and wind direction are 10 knots and 320°, respectively. The rest of The Netherlands had wind speeds around 5 knots with a northerly wind (360°-10°).

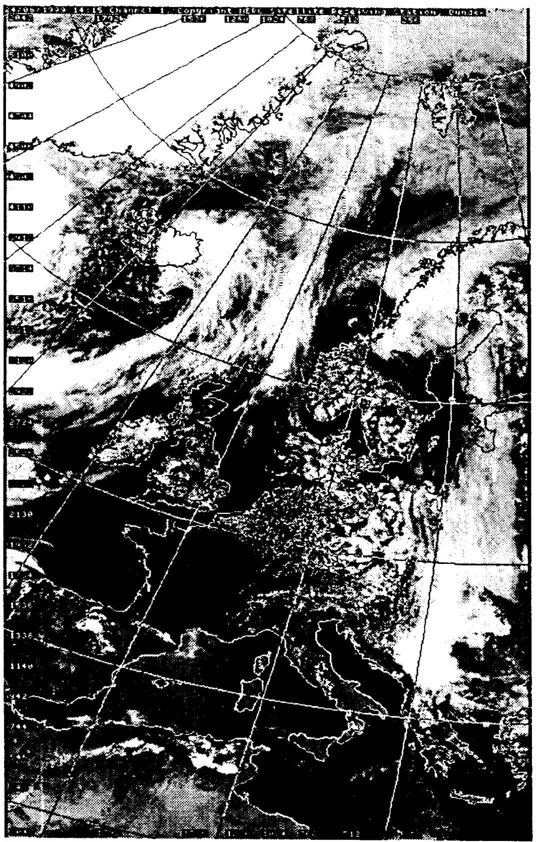

Figure 4.26a: AVHRR channel 4 image Europe at 14:13 UTC on 24 June 1999 (DUNDEE).

Figure 4.26b: AVHRR channel 4 image of Europe at 14:13 UTC on 24 June 1999 (DUNDEE).

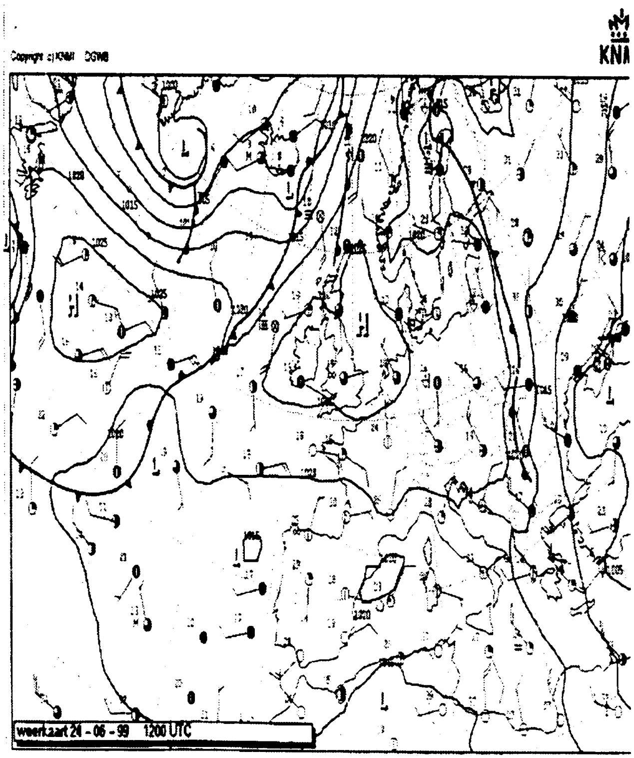

Figure 4.27: Weather map of Europe valid for 12:00 UTC on 24 June 1999.

Figure 4.28: AVHRR channel 1 image of The Netherlands at 14:13 UTC on 24 June 1999 (KLAROS).

b) Comparison of Retrieval Results

Results in Fig. 4.29 show measured DSSI obtained from upward looking pyranometers and those retrieved from the downward looking AVHRR instrument onboard the NOAA-14 satellite. The purpose of this figure is to explain the most important processes responsible for the random and systematic errors seen in this figure and to explain the influence of broken clouds on the RTM in general. It is important to stress that differences between measured and retrieved quantities are not automatically due to retrieval deficiencies. Also physical uncertainties arise due to *changing* physical quantities, such as changes in the observed cloud atmosphere (i.e., cloud cover, Mie scattering) and calibration changes of pyranometers and the AVHRR. To overcome these physical uncertainties, the averaging period from point measurement (i.e. pyranometer measurements) has to be sufficiently long to provide a reasonable sampling of the mean irradiance corresponding to the region used in the satellite analysis, and the region has to be chosen large enough to minimize the influence of 3D effects.

Due to the different nature of expected error sources, we try to make a distinction between physical uncertainties and retrieval deficiencies.

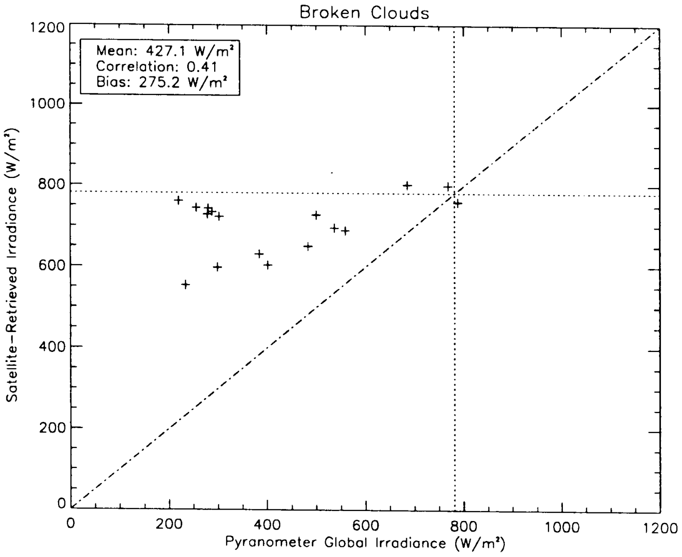

Figure 4.29: Comparison of Downwelling Solar Shortwave Irradiance for all pyranometer measurements available for a single satellite overpass on 24 June 1999. The vertical and horizontal bar (dashed line) illustrates the DSSI in case of clear sky.

Physical uncertainties

Several sources of physical uncertainties arise concerning broken cloud fields. An important mechanism is the development rate of a cumulus cloud. Cumuli have a lifetime in the order of tens of minutes (Feijt, 2000). This variability is fundamental to cloud processes and therefore, it is expected that the development rate of the observed cumuli is mostly responsible of the time dependency to global irradiance measurements at the surface. This is also part of the collocation problem, which plays an important role in cases with heterogeneous clouds (see Sec. 4.1). If a cloud field has low spatial and temporal variability, the measurement at one pyranometer site is representative for a large area. However, in a cumulus field the amount of downwelling shortwave irradiance measured at the surface is highly variable. As the size of a cumulus cloud change, also will the amount of downwelling solar irradiance falling on the pyranometers. This variability is much less accounted for by the instantaneous field of view (IFOV) of the AVHRR instrument. A cloud mask is used to classify pixels to be cloud filled or cloud free. Pixels are classified cloud free when the measured bi-directional reflectivity, as seen within the AVHRR 0.63 μm spectral band, is below a threshold value, which is 10% for narrowband measurements. The observed cumuli field is evenly distributed for a significant part of The Netherlands (see Fig. 3.28). It is therefore expected that the IFOV does not significantly change by different spatial scales.

Fig. 4.30 and 4.31 shows the influence of variability in measured and retrieved DSSI due to changes in temporal and spatial averaging scales. As for Fig. 4.30, random scatter show that pyranometer measurements are sensitive for changes in time interval. This is due to statistically averaging the period in which pyranometer measurements are carried out. For a 70-minute averaging period, peak measurements of solar irradiance are statistically more spread out than for a 10-minute averaging period. Results plotted in Fig. 4.31 shows less sensitivity in changes in averaging scale than in Fig. 4.30. This is expected, as mentioned above. The random scatter is of much smaller scale than shown in Fig. 4.30. The retrieved DSSI are concentrated at the high end of the one-to-one line. Values exceeding the clear-sky value (i.e. indicated by a vertical and horizontal dashed line) are likely caused by a small difference in calculations of the solar zenith angle (see Fig. 4.9a).

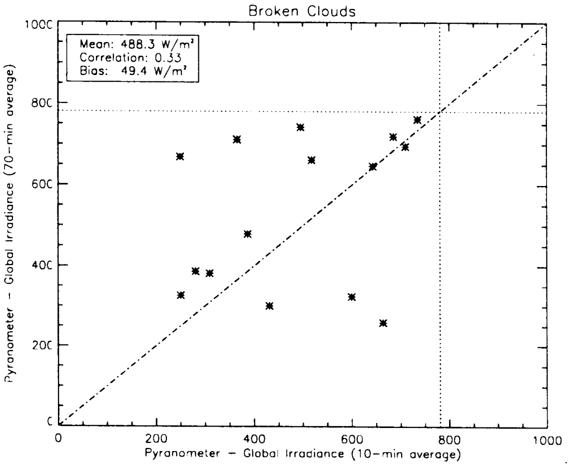

Figure 4.30: Global irradiance measured by pyranometers as function of time interval in case of broken clouds. The vertical and horizontal bar represent the DSSI in case of a clear sky.

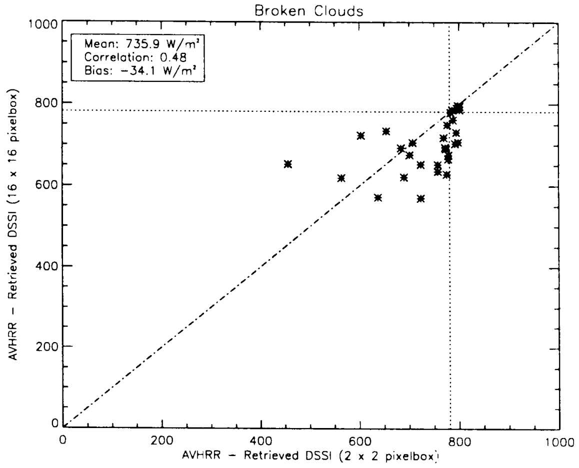

Figure 4.31: As in Fig. 4.30, except that the averaging scales are spatially varied.

According to the signature of the observed cloud field, it is appropriate to say that the different signature between Fig. 4.30 and 4.31 is also due to the existence of sub pixel clouds. The smallest AVHRR pixel resolution is 1.1 x 1.1 km, whereas the cumulus cloud may be much smaller. It is therefore possible that a pixel is labelled cloud free, while there are actually some clouds within the FOV of the pyranometer. Hence, the retrieval scheme would be overestimating the downwelling solar surface irradiance.

Another aspect concerning the collocation problem is a possible mismatch in the geolocation of the pyranometer sites as seen by the AVHRR. In case of small cloud fractions, some pixels in the vicinity of the pyranometer site may contain clouds, while others are clear. For perfect collocation, it should be known in which AVHRR pixels clouds are observed. Obviously, this information is not at hand. Therefore the probability that a cloud was present in a pixel at a distance from the pyranometer site must be estimated.

The mechanisms outlined above needs to be accounted for in a quantitative estimate of retrieval performance, as it is completely independent of retrieval deficiencies. A detailed analysis of the spatial and temporal scaling properties of the DSSI is required for this (see Feijt, 2000 and Jolivet, 1999), which is beyond the scope of this study.

Retrieval deficiencies

A limitation of both pyranometer and satellite retrieval which is important in case of broken clouds, is the assumption of a spectral invariant surface albedo. The differences of typical spectral dependence of the surface albedo for vegetation are close to one percent in atmospheric transmissivity (Deneke, 2002). The albedo is small for wavelengths below 0.63 μm, and increases significantly at the red edge around 0.7 μm. Due to the wavelength dependency of the surface albedo, assuming a *spectrally invariant* albedo value, which is closest to the real surface albedo, is difficult.

Fig. 4.32 shows the comparison between measured AVHRR channel 1 bi-directional reflectivities and pixel boxes obtained at KNMI station 'Volkel'.

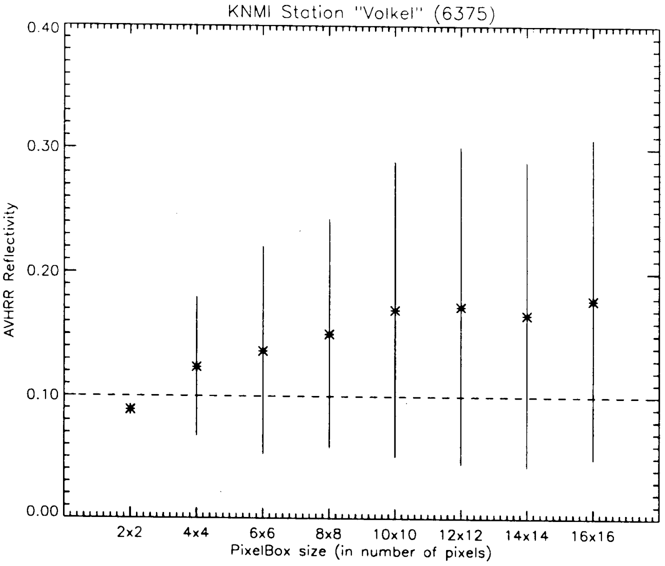

Figure 4.32: Relationship between the box size and the average and its standard deviation (vertical bars) of NOAA-14 AVHRR obtained bi-directional reflectivity around Volkel, The Netherlands. The dashed line represents the reflectivity value, set as threshold in the satellite retrieval.

An increase in reflectivity is seen when pixel boxes are increased. The smallest box of 2 x 2 pixels shows a reflectivity value that is lower than the threshold reflectivity of 10% assumed in the satellite retrieval. Below this threshold, pixels are classified as cloud free. The STD of the 2 x 2 pixel box is very small and therefore not detectable. This indicates homogenous surface characteristics around the measurement site. By increasing the pixel boxes, the STD increases as well. This is expected, because large pixel boxes will represent large areas. Hence, the surface will presumable be more heterogeneous. Also the influence of the broken cloud field becomes more important when the size of the pixel box increases. Since clouds scatter more radiation than the assumed surface albedo of 10% for narrowband measurements, it is believed that this phenomenon is responsible for the increase in reflectivity shown in Fig. 4.32. Also an increase in STD is detected. This is mainly due to enhanced horizontal photon transport. In case of broken cloud fields, sides of the clouds are illuminated for solar zenith angles of $\theta_0 \neq 0^\circ$. A larger area, therefore, is illuminated than for PPH cloud. This enhanced illuminated area also influences the reflected radiation and depends on the actual size distribution as well as on cloud fraction (Kobayashi, 1989). The impact of horizontal transport can be detected when calculated atmospheric transmissivities are above unity.

c) Conclusions

Comparing DSSI in case of broken clouds does not yield unambiguous information on the quality of the retrievals schemes. When comparing ground and satellite quantities, measured or retrieved, it is always questionable which part of the time series corresponds to which part of the spatial distribution. The observed deviations between pyranometer measured and satellite retrieved DSSI are of fundamental nature, as the static view of a cloud field assumed in the retrievals does not reflect all aspects of the observed broken cloud field. Broken clouds show significant variability in time and space (4D). Knowledge of surface characteristics is important for determining the effects of the horizontal photon transport and the enhanced illumination. However, 4D effects are difficult to interpret within the boundaries of a 1D radiative transfer model, used in this thesis.

5. Discussion and Conclusions

The aim of this research is to analyse the accuracy of downwelling solar surface irradiance (DSSI) retrieval schemes for satellites with *in situ* pyranometer measurements. Therefore, three cases are selected on their cloud cover fraction and referred to as 'clear-sky', 'overcast', and 'broken clouds'.

As for the clear sky case, the correspondence between the satellite retrieved and ground-based measured DSSI is generally good, yielding a small bias of 2.9 W m^{-2} (after correction for the offset in calculating solar zenith angles). The latter is only 0.4% of the mean irradiance. The corrected bias of the retrieval results remains within the boundaries of the estimated pyranometer calibration accuracy of 5%. We have further noted a higher variability of atmospheric transmissivity in the pyranometer measurements than in the output of the satellite retrieval. We found a RMSE of 0.017 that is 2.3% of the mean BAT. This is possibly related to the representation of spatial variability of atmospheric constituents that are not accounted for in the RTM. This is a limitation, since spatial variation in IWV and aerosol concentration can lead to significant deviation in retrieving DSSI. However, this limitation also marks the boundary conditions of the satellite retrieval. With respect to the required assumptions in the RTM, several detailed parameters are not taken into account, e.g. variant surface albedo, calibration errors of the ground-based pyranometer and possible presence of sub grid cloud fractions. The impact of these effects on the results is not known. The impact of possible cloud contamination and calibration errors on the results is not known.

The analysis of the overcast case shows a large difference in skill of the retrieval schemes between precipitation and non-precipitation cases. Therefore, discrimination of non-precipitating and precipitation cases is desirable for comparison of retrieved values with ground-based pyranometer measurements. As for the non-precipitation case, the retrieval is capable of capturing the observed cloud layer, resulting in a correlation coefficient of 0.89 and a bias of 12.4 W m^{-2}. The latter is 9.6% of the mean. However, for the precipitation case, the comparison between satellite retrieved and pyranometer measured DSSI does not show any correlation. A number of possible explanations for the observed discrepancies are classification of the cloud phase, absorption characteristics in the RTM, and contamination of the pyranometer domes during rainfall. Realistic values of IR temperatures show the presence of both water droplets and ice crystals at cloud top. Since the RTM does not account for mixed-phase clouds, errors are expected in form of noise and bias due to this limitation. Furthermore, a significant loss in accuracy of RTM in form of bias is expected if rain events occur. Rain droplets absorb more in the NIR of the solar spectrum than small cloud particles. There is no assumption in the RTM in its current form, which accounts for the absorption characteristics of rain droplets. Quantifying the effect of the contamination of pyranometer domes is desirable, since the impact on measurements is not thoroughly understood. For future research, it is recommended to use additional instruments for discriminating precipitation from non-precipitation conditions (e.g. Doppler radar). It is expected that with this discrimination the retrievals will increase in accuracy significantly.

Comparing DSSI in case of broken clouds does not yield unambiguous information on the quality of the retrievals schemes. When comparing ground and satellite quantities, measured or retrieved, it is always questionable which part of the time series corresponds to which part of the spatial distribution. The observed deviations between pyranometer measured and satellite retrieved DSSI are of fundamental nature, as the static view of a cloud field assumed in the retrievals does not reflect all aspects of the observed broken cloud field. Broken clouds show significant variability in time and space (4D). Knowledge of surface characteristics is important for determining the effects of the horizontal photon transport and the enhanced illumination. However, 4D effects are difficult to interpret within the boundaries of a 1D radiative transfer model, used in this thesis.

Acknowledgements

I would like to thank Prof Dr. Bert Holtslag for his suggestions, criticism, and advice on the general direction. Also I would like to thank Dr. Rose Dlhopolsky and Dr. Hartwig Deneke for their support on data analysis and UNIX/ IDL programming.

Gerben van Geel
De Bilt, April 2003

Appendix A

Acronyms and Physical Constants

Acronyms

APOLLO	AVHRR Processing scheme Over cLoud, Land and Ocean
AVHRR	Advanced Very High Resolution Radiometer
BAT	Broad-band Atmospheric Transmissivity
DSSI	Downward Solar Surface Irradiance
HIRLAM	HIgh Resolution Limited Area Model
IDL	Interactive Data Language
IFOV	Instantaneous Field Of View
KLAROS	KNMI Local implementation of APOLLO Retrievals in an Operational System
LW	Long Wave
LWP	Liquid Water Path
NIR	Near InfraRed
NOAA	National Oceanographic and Atmospheric Administration
NWP	Numerical Weather Prediction model
RTC	Radiative Transfer Code
RTM	Radiative Transfer Model
STD	Standard Deviation
SW	Short Wave
TOA	Top Of the Atmosphere

Physical Constants

Stefan-Boltzmann constant, σ	5.67032×10^{-8} W · m^{-2} · K^{-4}
Speed of light in vacuum, *c*	2.997925×10^{8} m · s^{-1}
Planck's constant, *h*	6.626196×10^{-34} J · s
Solar constant, *S*	1,367 ± 5 W · m^{-2}

Appendix B

Albedo for different terrain types

Vegetation/ Surface	*Remarks*	*Albedo*
Crops		
	Green grass	0.26
	Dry grass	0.15-0.25
	Maize	0.16-0.23
	Winter Rye	0.21
	Summer Rye	0.15-0.18
	Wheat	0.10-0.25
	Barley	0.26
	Potatoes	0.15-0.25
	Lettuce	0.22
	Sugar Beets	0.18-0.25
Forest		
	Coniferous	0.10-0.14
	Deciduous	0.10-0.19
Snow		
	Fresh	0.82-0.99
	Old	0.40-0.50
Uncultivated farmland		
	Clay	0.16-0.23
	Humus (dark & coarse)	0.05-0.10
	Sand (grey & dry)	0.25
	Sand (grey & moisture)	0.18
	Sand (light coloured & fine)	0.37
	Sand (wet)	0.09
Water		
	Cloudy atmosphere	0.06
	Low Sun	0.10-1.00
	High Sun	0.03-0.10

Table B: Albedo for different terrain types. Source: De Bruin, 1998.

Appendix C

Pyranometer Stations

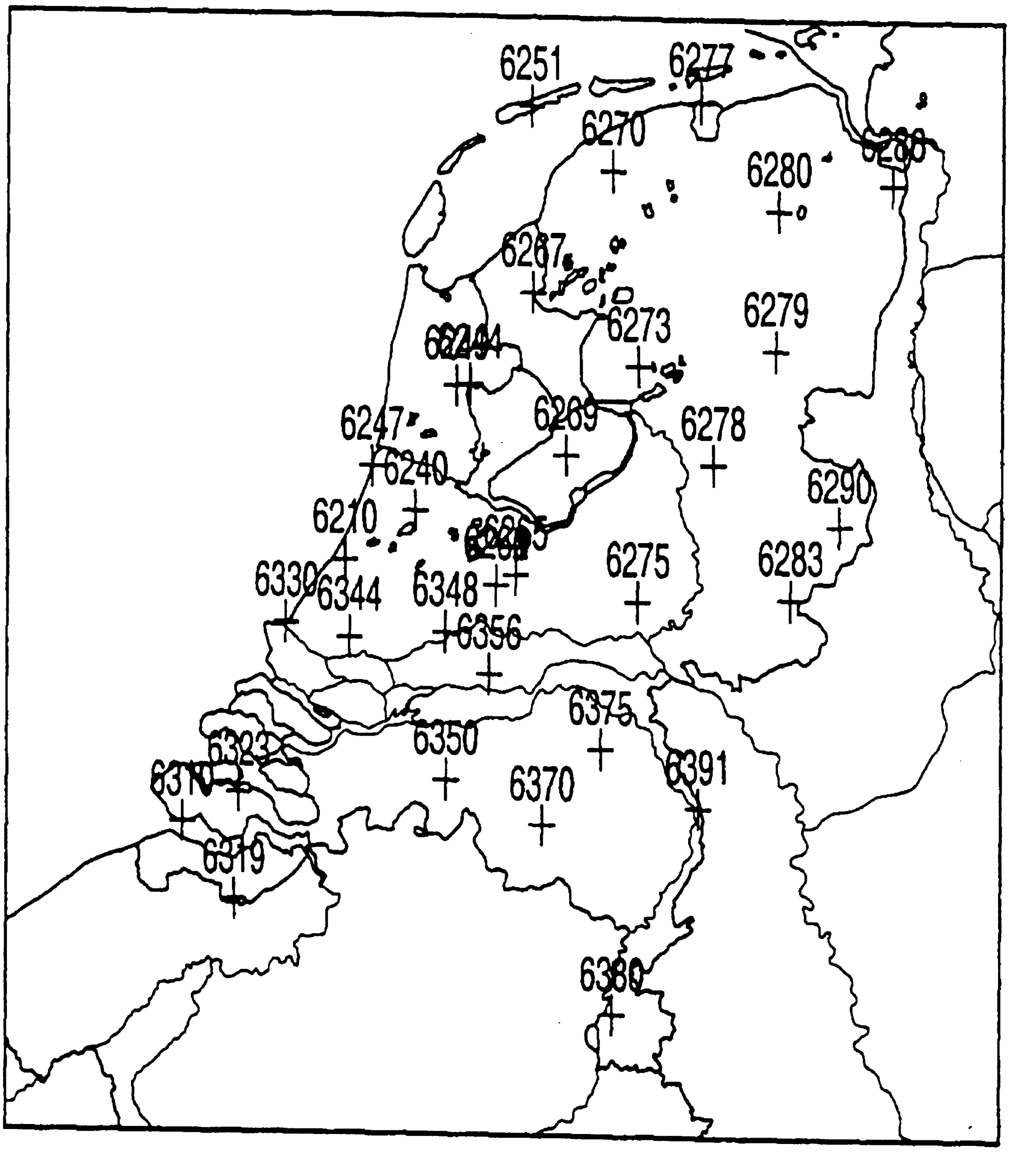

Figure C: Map showing the geographic location (+) of KNMI's meteorological measurement sites equipped with a pyranometer.

Number	*Name*	*Latitude*	*Longitude*	*Synop*
6210	Valkenburg	52.1650	4.4192	yes
6240	Schiphol	52.3014	4.7742	yes
6244	Hoorn AWS (NH)	52.6496	5.0444	no
6247	Bloemendaal	52.4216	4.5555	no
6249	Berkhout	52.6440	4.9791	no
6251	Hoorn AWS (Terschelling)	53.3928	5.3455	no
6260	De Bilt	52.1009	5.1774	yes
6265	Soesterberg	52.1298	5.2744	yes
6267	Stavoren AWS	52.8979	5.3557	no
6269	Lelystad AWS	52.4576	5.5260	no
6270	Leeuwarden	53.2251	5.7545	yes
6273	Marknesse	52.7032	5.8885	no
6275	Deelen	52.0609	5.8878	yes
6277	Lauwersoog	53.4092	6.1959	no
6278	Heino	52.4372	6.2636	no
6279	Hoogeveen	52.7502	6.5745	yes
6280	Eelde	53.1254	6.5858	yes
6283	Hupsel	52.0730	6.6495	no
6286	Nieuw Beerta	53.1962	7.1501	no
6290	Twenthe	52.2725	6.8896	yes
6310	Vlissingen	51.4424	3.5961	yes
6319	Westdorpe	51.2256	3.8616	no
6323	Wilhelminadorp AWS	51.5271	3.8840	no
6330	Hoek van Holland	51.9925	4.1238	yes
6344	Rotterdam	51.9546	4.4437	yes
6348	Cabauw	51.9717	4.9270	no
6350	Gilze-Rijen	51.5677	4.9332	yes
6356	Herwijnen	51.8584	5.1452	no
6370	Eindhoven	51.4455	5.4135	yes
6375	Volkel	51.6568	5.7056	yes
6380	Maastricht Airport	50.9104	5.7680	yes
6391	Arcen	51.4985	6.1957	no

Table C: WMO Number, station name, and geographic coordinates of KNMI's measurement stations equipped with a pyranometer. Also indicated is the availability of synoptical cloud reports.

Appendix D

Flow diagram of KLAROS

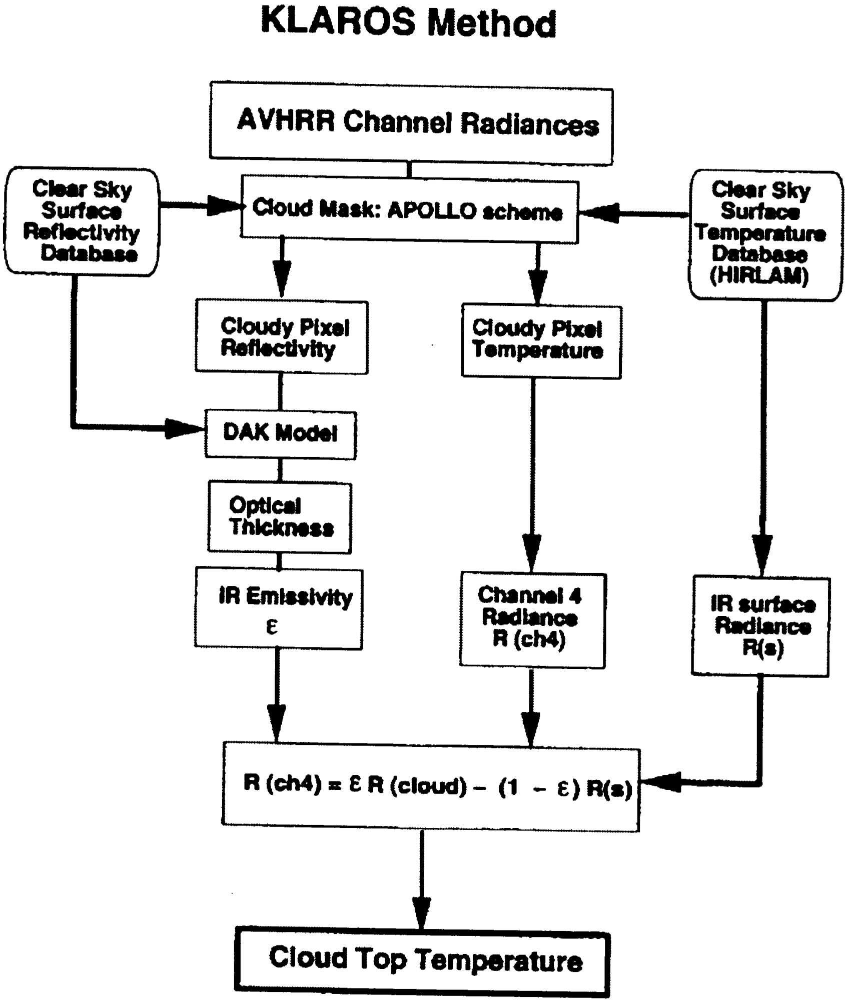

Figure D: Flow diagram of KLAROS method of cloud detection and property retrieval (Dlhopolsky & Feijt, 2001).

Bibliography

Barker, H.W. *et al.* (1998). Optical Depth of Overcast Cloud across Canada: Estimates Based on Surface Pyranometer and Satellite Measurements. *Journal of Climate*, Vol. **11**: pp. 2,980-2,894.

Boers, R., A. van Lammeren and A. Feijt (2000). Accuracy of Cloud Optical Depth Retrievals from Ground-Based Pyranometers. *Journal of Atmospheric and Oceanic Technology*, Vol. **17**: pp. 916-927.

Boers, R. and L.D. Rotstayn (2001). Possible links between cloud optical depth and effective radius in remote sensing observations. *Quarterly Journal of the Royal Meteorological Society*, Vol. **127**: pp.1-17.

Bréon, F.M., R. Frouin and C. Gautier (1994). Global Shortwave Energy Budget at the Earth's Surface from ERBE Observations. *Journal of Climate*, Vol. **7**: pp. 309-324.

De Bruin, H.A.R. (1998). Micrometeorologie. Vakgroep Meteorologie. Landbouwuniversiteit Wageningen, Wageningen.

Cess, R.D. *et al.* (1996). Absorption of solar radiation by clouds: Interpretations of satellite, surface, and aircraft measurements. *Journal of Geophysical Research*, Vol. **101**: pp. 23,299-23,309.

Cotton, W.R. and R.A. Anthes (1989). *Storm and Cloud Dynamics*. Geophysics Series No. 44; pp.148-186. Academic Press, San Diego, Ca.

Deneke, H.M. (2002). *Influence of Clouds on the Solar Radiation Budget* (dissertation). KNMI, De Bilt.

Dlhopolsky, R. and A.J. Feijt (2001). *Cloud products retrieval for MSG*. BCRS-Report USP2 00-34, BCRS, Delft.

Fanning, D.W. (1997). *IDL Programming Techniques*. Fanning Software Consulting, Fort Collins, CO USA.

Feijt, A.J. (2000). *Quantitative Cloud Analysis using Meteorological Satellites* (dissertation). KNMI, De Bilt.

Feijt, A.J. and H. Jonker (2000). Comparison of scaling parameters from spatial and temporal distributions of cloud properties. *Journal of geophysical research.*. Vol. **105**, No. D23: pp. 29,089-29,097.

Feijt, A.J., D. Jolivet and E. van Meijgaard (2002). Retrieval of the spatial distribution of liquid water path from combined ground-based and satellite observations for atmospheric model evaluation. *Boreal Environment Research,* Vol. **7**: pp. 265-271.

Goody, R.M. and Y.L. Yung (1989). *Atmospheric Radiation: Theoretical Basis*. New York: Oxford University Press.

Harris, R. (1987). *Satellite Remote Sensing: an introduction*. London/New York: Routledge & Kegan Paul.

Hobbs, P.V. (1993). *Aerosol-Cloud-Climate Interactions*. Academic Press, Inc. San Diego, California.

Hulst, H.C. van de (1957). *Light scattering by Small Particles*. New York: Dover Publications, Inc.

Jolivet, D. (1999). Etude de l'influence de l'heterogeneite des nuages sur le champ de rayonnement solaire réfléchi vers l'espace. Univ. of Lille, France.

Key, J. R. (1999). *Streamer User's Guide. Technical Report 96-01.* Dep. of Geography, Boston University, Boston.

Kidwell, K.B. (1998). NOAA polar orbiter data (POD) user's guide. Technical report, National Oceanic and Atmospheric Administration, Suitland, USA. Available from http://www2.ncdc.noaa.gov/docs/podug/.

Kiehl, J.T. and Kevin E. Trenberth (1997). Earth's Annual Global Mean Energy Budget. *Bulletin of the American Meteorological Society*, Vol. **78**, No. 2: pp. 197-208. Available from http://www.grida.no/climate/ipcc_tar/wg1/fig1-2.htm

Kyle, T.G. (1991). Atmospheric Transmission, Emission & Scattering. Oxford/ New York/ Seoul/ Tokyo: Pergamon Press.

Kobayashi, T. (1989). Radiative Properties of Finite Cloud Fields over a Reflecting Surface. *Journal of the Atmospheric Sciences*, Vol. **46**: pp. 2,208-2,214.

Lenoble, J.(1993). *Atmospheric Radiative Transfer*. Hampton, Virginia: A. Deepak Publishing.

Liou, K.N. (1980). *An introduction to Atmospheric Radiation*. International Geophysics series, Vol. **26**. New York: Academic Press Inc.

Liou, K.N. (2002). *An introduction to Atmospheric Radiation*. International Geophysics series, Vol. **84**. New York: Academic Press Inc.

Peixoto, J.P. and A.H. Oort (1992). *Physics of Climate*. New York: American Institute of Physics.

Pinker, R.T., R. Frouin and Z. Li (1995). A review of Satellite Methods to Derive Surface Shortwave Irradiance. *Remote Sensing of Environment,* Vol. **51**: pp. 108-124.

Pinker, R.T. and I. Laszlo (1992). Modelling Surface Solar Irradiance for Satellite Applications on a Global Scale. *Journal of Applied. Meteorology*, Vol. **31**, No. 2: pp. 194-211.

Russell, P.B. *et al.* (2002). Comparison of Aerosol Single Scattering Albedos Derived by Diverse Techniques in Two North Atlantic Experiments. *Journal of the Atmospheric Sciences*, Vol. **59**: pp. 609-619.

Saraber, M.J.M. (2000). *Satelliet meteorologie.* Lsg. Meteorologie en Luchtkwaliteit, Wageningen Universiteit. Wageningen.

Saunders, R.W. and K.T. Kriebel (1988). An improved method for detecting clear sky and cloudy radiances from AVHRR data. *International Journal of Remote Sensing*, Vol. **9**: pp.123-150.

Thomas, G.E. and K. Stamnes (1999). *Radiative Transfer in the Atmosphere and Ocean*. Cambridge: University Press.

Internet sites:

http://www2.ncdc.noaa.gov/docs/podug/

http://www.shef.ac.uk/misc/personal/bryant/lect4

http://earthobservatory.nasa.gov/Study/CloudsInBalance/

http://idlastro.gsfc.nasa.gov/homepage.html

http://www.astro.washington.edu/deutsch/idl/htmlhelp/index.html

Regen maakt het landschap wakker
Dan komt alles om je heen tot leven
Kleuren en geuren strijden om je aandacht
En het enige wat je hoort
Is hoe de hemel de aarde raakt.

-National Geographic-